

**Showcasing results from the ELIBIO project. A joint venture between Czech Academy of Sciences' Institutes of Biotechnology and Physics utilising the European Extreme Light Infrastructure (ELI Beamlines) facility.**

Femtosecond-to-nanosecond dynamics of flavin mononucleotide monitored by stimulated Raman spectroscopy and simulations

The research published is part of the ELIBIO programme on "Structural dynamics of biomolecular systems". The aim of ELIBIO is to create breakthrough science in biology, chemistry, and physics across multiple length and time scales by exploring new frontiers in light and optics using unique lasers. The current results track the ultrafast excited-state dynamics of free FMN. This opens up new avenues of investigation for flavins embedded in proteins.

**As featured in:**



See Prokopić C. Andrikopoulos, Gustavo Fuertes *et al.*, *Phys. Chem. Chem. Phys.*, 2020, 22, 6538.

## PAPER



Cite this: *Phys. Chem. Chem. Phys.*,  
2020, 22, 6538

# Femtosecond-to-nanosecond dynamics of flavin mononucleotide monitored by stimulated Raman spectroscopy and simulations†

Prokopis C. Andrikopoulos,<sup>‡\*</sup> Yingliang Liu,<sup>‡\*</sup> Alessandra Picchiotti,<sup>‡\*</sup> Nils Lenngren,<sup>‡\*</sup> Miroslav Kloz,<sup>‡\*</sup> Aditya S. Chaudhari,<sup>a</sup> Martin Precek,<sup>b</sup> Mateusz Rebarz,<sup>b</sup> Jakob Andreasson,<sup>b,c</sup> Janos Hajdu,<sup>b,d</sup> Bohdan Schneider<sup>a</sup> and Gustavo Fuenes<sup>a</sup>

Flavin mononucleotide (FMN) belongs to the large family of flavins, ubiquitous yellow-coloured biological chromophores that contain an isoalloxazine ring system. As a cofactor in flavoproteins, it is found in various enzymes and photosensory receptors, like those featuring the light-oxygen-voltage (LOV) domain. The photocycle of FMN is triggered by blue light and proceeds via a cascade of intermediate states. In this work, we have studied isolated FMN in an aqueous solution in order to elucidate the intrinsic electronic and vibrational changes of the chromophore upon excitation. The ultrafast transitions of excited FMN were monitored through the joint use of femtosecond stimulated Raman spectroscopy (FSRS) and transient absorption spectroscopy encompassing a time window between 0 ps and 6 ns with 50 fs time resolution. Global analysis of the obtained transient visible absorption and transient Raman spectra in combination with extensive quantum chemistry calculations identified unambiguously the singlet and triplet FMN populations and addressed solvent dynamics effects. The good agreement between the experimental and theoretical spectra facilitated the assignment of electronic transitions and vibrations. Our results represent the first steps towards more complex experiments aimed at tracking structural changes of FMN embedded in light-inducible proteins upon photoexcitation.

Received 4th September 2019,  
Accepted 22nd January 2020

DOI: 10.1039/c9cp04918e

rsc.li/pccp

## 1. Introduction

Flavins are important chromophores that elicit biological functions either alone or as part of enzymes and photosensory proteins.<sup>1</sup> Flavin-binding photoreceptors include the light-oxygen-voltage (LOV) domains,<sup>2</sup> the sensors of blue light using FAD (BLUF)<sup>3</sup> and cryptochromes.<sup>4</sup> Interest in such blue-light-sensitive sensory photoreceptors is increasing as they serve as building blocks in optogenetics and synthetic biology applications.<sup>5</sup> Since the molecular mechanism of action of flavoproteins relies on flavin

photochemistry, a detailed understanding of the flavin photocycle is essential to further the field. The large family of flavins, containing a dimethyl-substituted isoalloxazine ring system, includes flavin mononucleotide (FMN) which is the subject of this study (Fig. 1), flavin adenine dinucleotide (FAD), riboflavin (or vitamin B<sub>2</sub>) and its photolysis product lumiflavin. The latter two members as well as the riboflavin analogue roseoflavin<sup>6,7</sup> are typical systems to study computationally<sup>7–11</sup> and experimentally,<sup>12,13</sup> being less substituted in the N<sub>10</sub> position than FMN/FAD,<sup>14–16</sup> which reduces the complexity and size of the system. Recently, a number of time-resolved electronic and vibrational spectroscopy studies have tried to tackle flavins either in isolation<sup>17–20</sup> or in their native protein environments.<sup>21–23</sup> Among various time-resolved techniques, femtosecond stimulated Raman spectroscopy (FSRS)<sup>24–27</sup> has the unique capability to observe the ultrafast evolution of biological chromophores upon optical excitation.<sup>28–32</sup> However, the use of FSRS to probe flavin photodynamics is still in its infancy.<sup>12,33</sup>

In short timescale experiments (0-up to 10 ns), flavin chromophores, either free in solution or within proteins, can be thought of as closed systems.<sup>19</sup> Further intermediates such as adduct

<sup>a</sup> Institute of Biotechnology of the Czech Academy of Sciences, BIOCEV, Průmyslová 595, CZ-252 50 Vestec, Czech Republic.

E-mail: Prokopis.Andrikopoulos@ibt.cas.cz, Gustavo.Fuenes@ibt.cas.cz

<sup>b</sup> Institute of Physics of the Czech Academy of Sciences, ELI Beamlines, Za Radnicí 835, CZ-252 41 Dolní Břežany, Czech Republic

<sup>c</sup> Condensed Matter Physics, Department of Physics, Chalmers University of Technology, 412 96 Gothenburg, Sweden

<sup>d</sup> Department of Cell and Molecular Biology, Uppsala University, Husargatan 3 (Box 596), SE-751 24 Uppsala, Sweden

† Electronic supplementary information (ESI) available. See DOI: 10.1039/c9cp04918e

‡ These authors contributed equally.

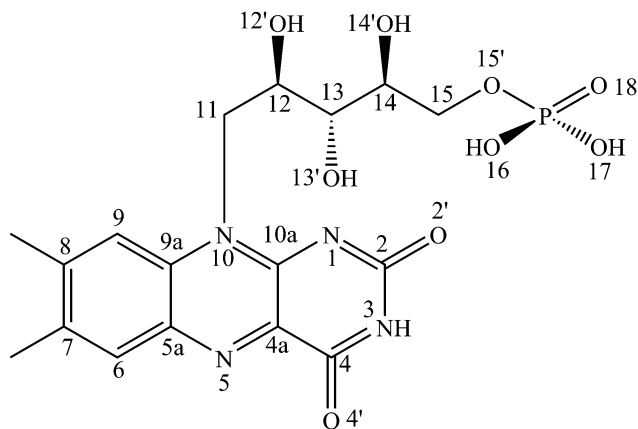


Fig. 1 Structure and numbering of flavin mononucleotide (FMN) in the neutral form.

formation or photooxidation/photoreduction products occur at longer timescales, so within the experimental time window, the fluorescing singlet system is only linked to a (phosphorescing) triplet. It is assumed that the initial hot states are depopulated within  $\sim 160$  fs to the  $S_1$  state *via* an internal conversion process (IC).<sup>34–36</sup> From there, within 5 ns, the system either fluoresces back to the ground state, or undergoes intersystem crossing (ISC) *via* an  $n\pi^*$  state to the first triplet ( $T_1$ ).<sup>37</sup> Then, depending on the pulse configuration of the experiment, higher triplet states become accessible,<sup>35</sup> or phosphorescence to the ground state ( $S_0$ ) occurs within several  $\mu\text{s}$ .<sup>35,38</sup> Triplet formation has typical quantum yield values of 0.61 [ $\geq 0.5$ ]<sup>39,40</sup> for riboflavin and a rate constant of  $7 \times 10^7 \text{ s}^{-1}$  [ $1.3 \times 10^8 \text{ s}^{-1}$ ] (values in brackets for isolated FMN).<sup>35,40</sup> The triplet-state population increases steadily along the duration of the experiment, with reported ISC timescales as fast as 2.8 ns in flavoproteins.<sup>41</sup> The photocycle of flavins inside protein cages is more elaborate. For instance, LOV proteins feature adduct formation between the excited FMN triplet state and a nearby cysteine residue, possibly with the involvement of radical intermediates.<sup>42–46</sup>

FMN in contrast to riboflavin and FAD carries additional complexity because of the free phosphate group. The charge of the phosphate moiety is pH-dependent, with  $pK_a$  values of 0.7 and 6.2 for the first and second deprotonation, respectively.<sup>47</sup> At extreme alkaline conditions (pH values over 10.2), the isoalloxazine  $N_3$  atom is also deprotonated to give a total FMN charge of  $-3$ . Therefore, at physiological pH values, FMN in solution is expected to have either  $-1$  or  $-2$  charge which is usually balanced by sodium cations. Additionally, the ribityl-phosphate chain of FMN is flexible enough to form intramolecular hydrogen bonds with the isoalloxazine ring atoms<sup>16</sup> competing for those with the solvent shell molecules.

The absorption spectra of free flavins display two characteristic bands at approximately  $\lambda_1 = 450$  nm and  $\lambda_2 = 350$  nm assigned to  $S_1$  and  $S_2$   $\pi\pi^*$  transitions, respectively. The transition from singlet to triplet state is postulated to be mediated by either singlet or triplet  $n\pi^*$  states located mainly on the heteroatom lone pairs of the isoalloxazine ring.<sup>18,37</sup> Recent contributions in the literature report accurate assignments of FSRS spectra by

theoretical calculations, either by relying on ground-state spectra or including resonance enhancements to the computed intensities.<sup>48–50</sup> To the best of our knowledge, no systematic study of FMN has been undertaken to date and encouraged by the above-mentioned works we present here a joint experimental and computational study of free FMN in an aqueous solution. Stationary UV-visible, time-resolved transient absorption, FSRS, and fluorescence spectroscopy experiments were carried out on FMN water samples. The pH dependence of FMN was probed with the inclusion of MES (pH = 6) and Tris (pH = 8) buffers in additional water samples and the results were interpreted with the aid of time-dependent density functional theory (TDDFT), real-time TDDFT (RT-TDDFT) and spin-orbit coupling (SOC) calculations. The extended (6 ns) time window of the experiments allowed the partial evolution of the FMN triplet species to be monitored by FSRS.

## 2. Methods

### 2.1. Experimental details

**2.1.1. Samples, conditions, pH *etc.*** FMN (riboflavin-5'-monophosphate sodium salt hydrate) was purchased from Cayman Chemical Company and used without further purification. The Tris and MES buffers were provided from Sigma-Aldrich. FMN samples were prepared from a 45 mM FMN stock solution dissolved in Milli-Q water (pH = 5.9). Two buffers were used to study the influence of pH: 10 mM Tris (pH 8.0) and 10 mM MES (pH 6.0). For visible TA and FSRS experiments, FMN was diluted to a final optical density appropriate for the experiment at 400 nm in 1 mm path-length cuvettes. Specifically, the OD at 400 nm was adjusted to 0.5 in case of the TA experiments, 1.0–1.5 or more for the FSRS experiments, and between 0.6 and 0.8 for the steady-state absorption experiments. For the fluorescence experiments, FMN was further diluted to 10  $\mu\text{M}$  to avoid the reabsorption effect. All experiments were conducted at 296 K.

**2.1.2. Raman and transient absorption (TA) setup.** The schematic layout in Fig. 2 represents the Raman setup employed in the current study, based on a similar setup described elsewhere.<sup>26,27</sup> The setup is pumped by a commercial Ti:Sapphire laser (Femtopower, Spectraphysics) that emits pulses centred at 800 nm with a pulse duration of  $\sim 20$  fs at a 1 kHz repetition rate.

The beam is split in three different paths, described as follows. In the FSRS experiments, as probe, a broad white light supercontinuum beam was employed, created by focusing the output of a home-built noncollinear optical parametric amplifier (NOPA) onto a sapphire plate. The 1400 nm driving pulse was suppressed by a dichroic filter. The resulting probe spectrum spans from 1400 nm to 380 nm and has a very flat spectral profile in the 800–1100 nm region, therefore allowing the detection of even very low Raman frequencies near the 800 nm Raman pump. This also applies for the high frequencies that are often obscured by low probe intensities. In our configuration where the 800 nm Raman signal was probed by the supercontinuum generated at 1400 nm, vibrations in the range of 60–3800  $\text{cm}^{-1}$  can be readily observed at the same time.

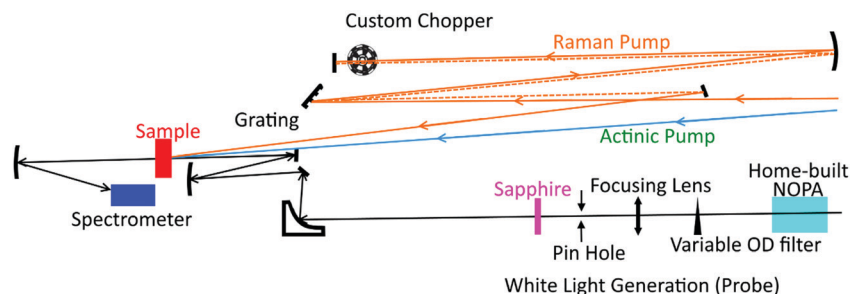


Fig. 2 Schematic layout of the stimulated Raman setup employed in this study with a folded-geometry 4-f pulse shaper in the Raman path.

The 400 nm actinic pump was generated by second harmonic generation (SHG) in a BBO crystal (Eksma) and adjusted to 2  $\mu\text{J}$  at the sample area. The Raman pump pulse was generated in a pulse shaper where a specially designed chopper blade acts as a wavelength-narrowing and wavelength-modulating element at the same time.<sup>27</sup> In this particular setup, 96 Raman pump wavelengths slightly shifted in the interval 760–840 nm were periodically recorded. The presented Raman spectra resulted from their recombination *via* a spectral watermarking approach.<sup>27</sup> The Raman pulse power was adjusted to be 3  $\mu\text{J}$  at the sample. The Raman pump and/or the actinic pulse were then focused and overlapped in the sample *via* a convex lens with 500 mm focal length. The probe pulse was focused by a concave spherical mirror with focal length 200 mm to ensure a smaller spot size. The Raman spectrum was resolved (red box in Fig. 2) by two commercial imaging spectrographs (Acton SP2150i) each observing half of the reported Raman spectrum with a spectral resolution of approximately 2  $\text{cm}^{-1}$ . The sample was circulated through a commercial pump (HNP Mikrosysteme) at a speed of 0.4  $\text{mL s}^{-1}$ , *i.e.*, 120  $\mu\text{m ms}^{-1}$  for the specific flow cell used below. This is ensuring that fresh sample is present for each new laser shot. The cuvette was a 1 mm path length thick quartz commercial flow cell (Hellma).

Transient absorption experiments were performed on a home-built set-up installed also at the ELI Beamlines laser facility. The main beam was split into excitation and probe beams by a dielectric beam splitter. The same pump and probe pulse source as in the FSRs experiment was used, however the white-light supercontinuum was generated in a 2 mm thick  $\text{CaF}_2$  plate that was continuously translated in the beam to ease the heat deposition in the generation spot. A dichroic mirror with 350–1064 nm reflectivity (Semrock) was used to partially separate the supercontinuum from the strong driving energy at 1400 nm that was mostly transmitted. The spectrum ranging from 350 to 1000 nm was resolved by a home-built quartz prism spectrograph that allowed imaging of the entire probe spectra on the detector array without overlapping higher-order diffractions that would happen with a grating spectrograph and otherwise prevent reliable recording of spectra beyond the full octave range (*e.g.* second-order diffraction at 500 nm overlaps with first-order diffraction at 1000 nm). Excitation and probe pulses were focused and overlapped on the sample with spot sizes measured to be about 40  $\mu\text{m}$  for the probe and about 120  $\mu\text{m}$  for the pump. The pump–probe polarization configuration was set at the magic

angle ( $54.7^\circ$ ). Two choppers for the probe (500 Hz) and pump (250 Hz) beams were used to record pumped and not pumped signal as well as to minimise the ambient and pump-related background. The temporal delay between pump and probe pulses was adjusted by a remote-controlled optical delay line inserted in the excitation path. For each delay the absorption-difference spectra ( $\Delta A$ ) were calculated and averaged over 500 pump pulses. The time window of the TA was 5 ns, while Raman spectra acquisition reached up to 6 ns.

**2.1.3. Stationary UV-vis, stationary and time-resolved fluorescence.** A spectrum of the sample before and after each time-resolved measurement was taken with a commercial spectrometer (UV-1900 Shimadzu), to ensure the sample was not damaged during the time-resolved experiment, and to provide the stationary spectra of the FMN samples that were used as reference. The stationary and time-resolved fluorescence spectra were measured with an Edinburgh Instruments FLS1000 fluorescence spectrometer. For the determination of fluorescent lifetimes *via* the time-correlated single photon counting (TCSPC) technique,<sup>51</sup> FMN was excited with a pulsed diode laser emitting at 405 nm. Fluorescence decays were fitted with a single exponential model in order to calculate the fluorescence lifetime ( $\tau_F$ ).

**2.1.4. Data analysis, methods and Glotaran.** A home-built software based on LabView was employed to read the signal from the spectrometers and a home-built software (written in Matlab) to transform it in order to extract the Raman spectra. Enough data were acquired to ensure appropriate statistics, typically twenty thousand spectra per each time point. The data were then averaged by wavelet processing<sup>26,27</sup> using a normalised Hadamard matrix as a basis set. The scaled and shifted pre-zero ground-state signal was subtracted from the difference Raman signal to correct for an artefact generated by Raman pulse scattering into the detected area. The residual background was then subtracted by fitting a polynomial with the least absolute value residual.

Global fitting of the transient absorption and transient Raman spectra was carried out with the Glotaran program (version 1.5.1).<sup>52</sup> A five-component sequential model was used to fit the transient spectra, of which the fast 0th component ( $\tau_0 < 100$  fs) is used to remove the coherent artefact generated when 400 and 800 nm pulses overlap in time. A long component of 10  $\mu\text{s}$ , corresponding to the phosphorescence lifetime of aqueous FMN,<sup>53</sup> is used to fit the non-decaying component lying outside the experimental time window (6 ns for FSRs and 5 ns for TA).

It proved non-trivial to separate the negative portion of the Raman signal from the excited positive signal, therefore it is excluded from the analysis.

## 2.2. Computational details

The initial model of FMN in its oxidised form was obtained from the crystal structure of the LOV protein EL222.<sup>54</sup> Subsequently, the molecule was treated with molecular dynamics (MD) with the Cuby4 program using an all-valence electron semi-empirical PM6-D3H4 potential<sup>55,56</sup> with the Berendsen thermostat algorithm<sup>57</sup> at a constant temperature of 300 K for 100 ps. A dielectric constant  $\epsilon$  of 78.3 was applied throughout the MD run approximating a water medium *via* the COSMO module.<sup>58</sup> The molecular dynamics were carried out on both the ground and the  $S_1$  state of FMN. The bulk of the calculations were performed with the Gaussian program (G16 Rev. B.01).<sup>59</sup> The hybrid B3LYP<sup>60,61</sup> and the def2-TZVP<sup>62,63</sup> combination of DFT functional and basis set was used. For all calculations dispersion corrections were included.<sup>64</sup> Solvation by water was applied *via* the polarisable continuum model (PCM)<sup>65-67</sup> for ground-state optimisations and through its implementation for excited states,<sup>68</sup> and non-equilibrium corrections *via* the external iteration scheme were added to the ground-state and fluorescence bands.<sup>69,70</sup> The non-equilibrium scheme employs an optical dielectric constant ( $n^2$ ) to the continuum instead of the actual dielectric constant ( $\epsilon$ ) to recalculate the point charges. These corrections give a better description to the very fast vertical processes of absorption and fluorescence where the electronic state of the solute changes rapidly to the new state while its nuclei and surrounding solvent molecules retain the previous state geometries. Vertical excitations, simulations of ground-state UV-vis spectra, and excited state optimisations were carried out with the TDDFT formalism with the same functional and basis set combination mentioned above and were solved for a total of forty states.<sup>68,71-73</sup> All but few of the excited-state optimisations located minima on the first  $S_1$  and  $S_2$  singlet excited-state potential energy surfaces (PES) of FMN as well as the first triplet excited state,  $T_1$ . The latter were performed by normal optimisation by setting the multiplicity to 3. Raman spectra were obtained for all stationary points located in the ground-state (GS) and excited-state PESS; pre-resonance Raman intensities were computed by solving the dynamic coupled-perturbed Hartree-Fock equations (CPHF).<sup>74,75</sup> For all Raman curves a half-width at half-height peak value of  $14 \text{ cm}^{-1}$  (HWHM) was used to match the experimental curve shapes (0.12 eV for absorption spectra), and all frequencies were scaled by 0.97 as per the recommended value for the level of theory and basis set.<sup>76</sup> The excited state absorption (ESA) was calculated *via* the real-time TDDFT method<sup>77</sup> as implemented in NWChem 6.8.1.<sup>78</sup> Excited state optimisations were repeated in NWChem for forty states at a more modest basis set (B3LYP-D/6-31G\*) without solvation corrections for both the  $S_1$  and  $S_2$  manifolds. An additional RT-TDDFT gradient calculation was performed on the  $S_1$  manifold with ground-state geometry to obtain a spectrum near the vertical excitation, which was corrected for zero field. All RT-TDDFT simulations were propagated for

$\sim 12$  fs with a time step of 0.2 a.u. using a delta function electric field with an intensity of 0.001 a.u. Extending the propagation to 24 fs or reducing the time step to 0.1 a.u. did not produce any visible differences in the spectra. Spin orbit coupling terms (SOCs) were computed for the  $S_0$ ,  $S_1$  and  $S_2$  geometries *via* the PySOC code<sup>79</sup> which was interfaced to the Gaussian outputs. PySOC calls the MolSOC code<sup>80</sup> to calculate the atomic integrals and evaluates SOCs between singlet and triplet states using the single-electron Breit-Pauli (BP) operator with an effective charge approximation.

Additionally, the protonation state of the phosphate group was sampled ranging from an overall neutral FMN for extremely acidic ( $\text{pH} < 0.7$ ), to doubly negative total charge for basic conditions ( $6.2 < \text{pH} < 10.7$ ).<sup>47</sup> For the models within the range  $0.7 < \text{pH} < 6.2$ , the total charge of the system was either left negative or balanced by a  $\text{Na}^+$  counter-ion to describe two distinctive solvation scenarios of the cation with respect to the FMN molecule.

## 3. Results and discussion

### 3.1. Transient absorption, excited-state calculations and fits

The stationary spectra used as a reference (Fig. 3c, bottom), show two absorption bands at 445 nm and 372 nm, assigned to  $S_0 \rightarrow S_1$  and  $S_0 \rightarrow S_2$  respectively, and the fluorescence spectrum displays a broad band at 528 nm typical of  $S_1 \rightarrow S_0$  emission. The chosen wavelength of the actinic pump at 400 nm ensured that adequate populations of both  $S_1$  and  $S_2$  states were reached, since it lies between their excitation wavelengths. At the given pump wavelength, 20 fs pulses produce a bandwidth wide enough to ensure this with a detectable FWHM of  $\sim 30$  nm. The transient absorption (TA) spectrum of FMN in  $\text{H}_2\text{O}$  is shown in Fig. 3a, with additional spectra of the  $\text{H}_2\text{O}:\text{MES}$  (pH 6) and  $\text{H}_2\text{O}:\text{Tris}$  (pH 8) samples included in the ESI† (Fig. S1). The different pH samples were prepared in order to determine the effect of altering the protonation state, and therefore the extent of negative charge, of the FMN phosphate group on the observed photodynamics. Global analysis of the raw TA data resolved five evolution-associated spectra (EAS) and its associated lifetimes ( $\tau$ ). The very first 0th component ( $\tau_0 < 100$  fs, not shown) was used to model the coherent artefact when pump and probe pulses overlap. The 1st component ( $\tau_1 = 0.6$  ps) is attributed to the delayed solvent response to the solute vertical excitation. A noticeable dynamical red-shift of the stimulated emission (SE) band between the 1st and 2nd components is typical of the  $S_1$ -state solvation process.<sup>53</sup> The 2nd and 3rd components are nearly identical in the measured spectral range but exhibit two very different time constants. A component such as the 2nd, at few tens of picoseconds, has been identified previously, and was assigned to minor relaxation processes in aqueous riboflavin.<sup>12</sup> The MD calculations showed that the folding/unfolding of the ribityl-phosphate moiety towards the isoalloxazine ring in FMN occurs within a 100 ps time window (Fig. S6, ESI†); then the 2nd component could be attributed to a hydrogen bond at the  $\text{N}_1$  position with a solvent molecule,

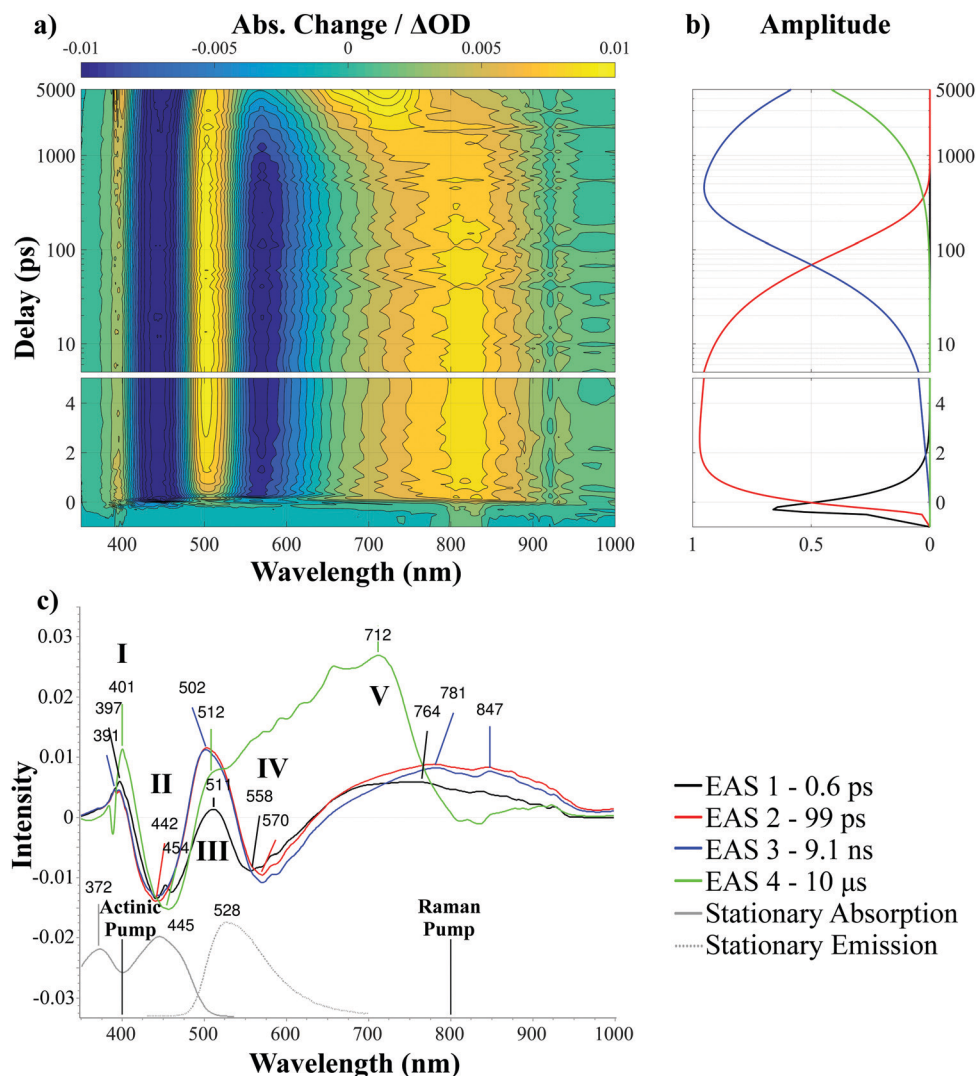


**Fig. 3** Transient absorption (TA) spectra of FMN in the unbuffered water solution, (a) TA contour plot at different delays after 400 nm photoexcitation. (b) Amplitudes from global fitting using a sequential kinetic scheme showing four components at  $\tau_1 = 0.6$  ps (black),  $\tau_2 = 100$  ps (red),  $\tau_3 = 9.1$  ns (blue), and the  $\tau_4 = 10$   $\mu$ s component (green). In (a) and (b) the time scale is linear up to 1 ps and logarithmic thereafter. (c) Evolution-associated spectra (EAS) of the latter four TA components plotted together with the stationary absorption (grey) and fluorescence (grey, dashed) spectra. The wavelengths of the Raman and actinic pumps are indicated with black lines. The most notable features of the TA described in the main text are labelled here with Latin capital numerals (I–V).

while the intramolecular  $O_{14'}-H \cdots N_1$  bond would be present in the 3rd component. The 3rd component represents the fully relaxed  $S_1$  state with a lifetime slightly outside the experimental window ( $\tau_3 = 9.1$  ns), whereas the 4th component's time constant was set to the phosphorescence lifetime of FMN ( $\tau_4 = 10$   $\mu$ s) and represents the non-decaying contribution within the time scale of the experiment.<sup>38</sup> The 4th EAS resembles very closely the lowest triplet absorption spectrum described in previous experiments on FMN and ribofavin<sup>53,81</sup> while the components 1st to 3rd describe different relaxation phases of the lowest singlet state. The plots of the latter four components are shown in Fig. 3c (top); the time constants from global fitting are included schematically in Fig. 3b and their values are listed in Table 1. Fixing the 3rd component to the fluorescent lifetime of FMN measured by time-resolved fluorescence spectroscopy ( $\tau_F = 4.8$  ns for the aqueous sample) yielded similar EAS (see

Fig. S2 for the measurement and Fig. S5a for the EAS comparison, ESI†) suggesting that the transient spectra of the 4th component are barely affected by possible errors in the determination of its lifetime.

The UV-visible TA spectra can be described by five distinct features (highlighted in Fig. 3c). Region I: the excited-state absorption (ESA) band around  $\sim 390$  nm progressively shifting to 401 nm in the last component. Region II: centred around 442 nm, the ground-state bleach (GSB), common for all components, which signifies diminishing ground-state ( $S_0$ ) population and corresponds to the stationary absorption 445 nm band; this band shifts to the red (454 nm) in the microsecond time scale. Region III: the broad  $S_1 \rightarrow S_n$  ESA band at  $\sim 511$  nm; This band blue-shifts by 9 nm in the late-ps-to-ns components as it increases in intensity from 1st to 3rd. Region IV: the below-baseline stimulated-emission band at 558–570 nm ( $S_1 \rightarrow S_0$ ) which is red-shifted but broadly corresponds to the spontaneous fluorescent band of the stationary

**Table 1** Time constants from global fitting of the transient absorption and Raman spectra. The 0th and 4th components were fixed during the fit. Other components were kept either fixed or free as indicated

EAS:	0th	1st	2nd	3rd	4th
Transient absorption fit					
H <sub>2</sub> O	67 fs <sup>a</sup>	0.6 ps	99 ps 120 ps <sup>b</sup>	9.1 ns 4.8 ns <sup>b</sup>	10 μs <sup>a</sup>
H <sub>2</sub> O:MES	67 fs <sup>a</sup>	0.9 ps	230 ps 226 ps <sup>b</sup>	4.7 ns 4.7 ns <sup>b</sup>	10 μs <sup>a</sup>
H <sub>2</sub> O:Tris	67 fs <sup>a</sup>	0.6 ps	108 ps 150 ps <sup>b</sup>	9.5 ns 4.7 ns <sup>b</sup>	10 μs <sup>a</sup>
Raman fit					
H <sub>2</sub> O	67 fs <sup>a</sup>	0.6 ps <sup>c</sup>	99 ps <sup>c</sup> 130 ps 140 ps <sup>b</sup>	9.1 ns <sup>c</sup> 4.8 ns <sup>b</sup>	10 μs <sup>a</sup>
H <sub>2</sub> O:MES	67 fs <sup>a</sup>	0.9 ps	100 ps 96 ps <sup>b</sup>	7.0 ns 4.7 ns <sup>b</sup>	10 μs <sup>a</sup>
H <sub>2</sub> O:Tris	67 fs <sup>a</sup>	0.6 ps <sup>c</sup> 0.9 ps 1.7 ps <sup>b</sup>	108 ps <sup>c</sup> 124 ps 120 ps <sup>b</sup>	7.2 ns 9.5 ns <sup>c</sup> 4.7 ns <sup>b</sup>	10 μs <sup>a</sup>

<sup>a</sup> Fixed values. <sup>b</sup> 3rd EAS fixed to the fluorescence lifetime of S<sub>1</sub>. <sup>c</sup> Fixed to the TA fit.

spectrum at 528 nm. Region V: the 700–900 nm region, where a broad band is present in components 1st to 3rd. In the last component (4th), it is replaced by another broad band with a maximum at 712 nm, which is intense due to the absence of SE. Such a broad band is pre-resonant with the Raman pump wavelength at 800 nm, which explains why excited-state FSRs signals are stronger than the ground-state signals. The H<sub>2</sub>O:MES and H<sub>2</sub>O:Tris samples produced almost identical EAS to the unbuffered sample only varying by their different lifetimes. Therefore, small variations of pH around neutrality do not significantly influence the evolution of excited FMN molecules.

Turning over to the computational results, as mentioned above, FMN displayed a rapid fold of the ribityl-phosphate moiety well within the 100 ps of the MD run. This occurred both for the ground-state and S<sub>1</sub> state simulations (Fig. S6, ESI<sup>†</sup>). After optimisation of the most stable structure obtained in the ground state, several models were devised to reflect the conditions of the samples studied experimentally (see description in the ESI<sup>†</sup> and Fig. S7). From those, models 2' and 2'' (Fig. 4) were chosen as default for comparison, to match the pH of the aqueous unbuffered sample (measured at 5.9). Optimisation of the Na<sup>+</sup>-balanced model (2'') resulted in a bidentate structure with equidistant contacts (2.4 Å) to the two unprotonated phosphate oxygens (Fig. 4, right). However, it is known from studies compiling crystal structure data that Na<sup>+</sup> prefers monodentate coordination to the negatively charged phosphate oxygen.<sup>82</sup> For this reason, analysis of 2'' was made in tandem with the unbalanced charge equivalent model 2' (Fig. 4, left). Ground-state UV-vis spectra were calculated for all the models of Fig. 4 and Fig. S7 (ESI<sup>†</sup>) and were compared to the stationary absorption spectrum. The computed excitation wavelengths to the S<sub>1</sub> and S<sub>2</sub> states are shown in Table 2, along with their oscillator strengths, participating orbitals, percentage contributions, excited state dipole moments and assignments. In a few of the models (2, 3), the S<sub>0</sub> → S<sub>2</sub> band was found to consist of two similar excitations, so the most intense of the two is given. The S<sub>0</sub> → S<sub>1</sub> excitation

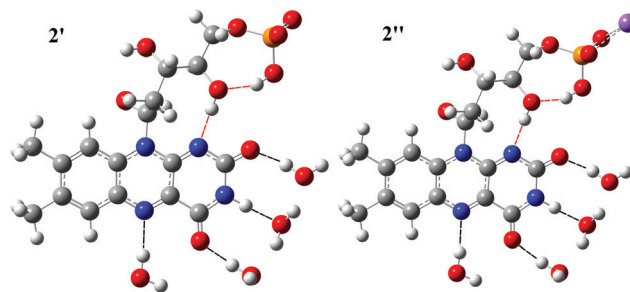


**Fig. 4** Structural models of micro-solvated FMN optimised in the water polarisable continuum (PCM) with B3LYP-D/def2-TZVP. The negatively charged model 2' with a deprotonated phosphate oxygen is shown on the left, and the Na<sup>+</sup>-balanced equivalent (2'') is shown on the right. The dashed red lines show the intramolecular hydrogen bonding network while the black the intermolecular. Atoms are coloured as follows, C: grey, H: white, N: blue, O: red, Na: violet.

measured experimentally at 445 nm was best matched by 2' and 3' with an error below 12 nm. With regards to the S<sub>2</sub> band, the spectra of all micro-solvated models deviate by less than 10 nm. The calculations of the neutral models 1, 1' and 2'' predicted larger dipole change  $|\Delta\vec{\mu}|$  in the S<sub>2</sub> than the S<sub>1</sub> transition, with 2'' being the closest to the experimental values for FMN.<sup>83</sup> An unbalanced charge in the phosphate group introduces a large error in the computed absolute  $|\vec{\mu}|$  and  $|\Delta\vec{\mu}|$  values (Table 2, models 2, 2', 3, and 3'). The percentage contributions of canonical orbitals involved in the two excitations are tabulated in the 6th and 7th columns of Table 2 (only excitations of over 2% are listed). Images of the orbitals are depicted in Fig. S8–S10 (ESI<sup>†</sup>) for the micro-solvated models. When the phosphate group carries a negative charge (2, 2') the excitations to the S<sub>1</sub> and S<sub>2</sub> states are predicted with increased nπ\* character, which in turn signifies a charge-transfer (CT) transition not present in the neutral, doubly negative or cation-balanced models (see description in the Section S3, ESI<sup>†</sup>). The described nπ\* states should not be confused with the nπ\* states involving lone pairs of the isoalloxazine ring heteroatoms which are reported to mediate the ISC in isoalloxazine systems.<sup>18,37</sup> Nevertheless, the possibility that the phosphate moiety can modulate the nπ\* character of the excited singlet state cannot be ruled out, which would be a unique feature of FMN. This statement is more supported by the computed spin-orbit coupling terms for the nπ\* states of 2'' which are presented further below, rather than the CT of the S<sub>1</sub> state which can be attributed to the self-interaction error of the unscreened phosphate charge in 2 and 2'. The singlet nπ\* states involving isoalloxazine heteroatom lone pairs are predicted to the blue of the S<sub>2</sub> band (351 and 353 nm for 2' and 2'', respectively) with oscillator strengths (*f*) close to 0. The equivalent triplet nπ\* states are calculated at 558 and 706 nm for 2' and 2'', respectively, again with very small *f* values. Other important triplet-triplet excitations will be highlighted in the following section.

An attempt to locate all stationary points in the excited state PES was made including all S<sub>1</sub>, S<sub>2</sub> (both S<sub>2</sub> excitations when applicable) and T<sub>1</sub> states. No excited singlet states were located for the 3' model with −2 charge, while the optimisation of the S<sub>2</sub> state of 3

**Table 2** Calculated vertical excitations  $\nu_e$  (in nm), oscillator strengths ( $f$ ), dominant orbitals with percentage contributions, excited state dipole moments  $|\bar{\mu}_1|$  and  $|\bar{\mu}_2|$  in Debye (with  $|\Delta\bar{\mu}|$  in brackets) and assignments. The relevant orbitals are depicted in Fig. S8–S10 (ESI)

	$\nu_e$ S <sub>1</sub>	$f$ (S <sub>1</sub> )	$\nu_e$ S <sub>2</sub>	$f$ (S <sub>2</sub> )	Orbitals S <sub>1</sub>	Orbitals S <sub>2</sub>	$ \bar{\mu}_1 $ [ $ \Delta\bar{\mu}_1 $ ]	$ \bar{\mu}_2 $ [ $ \Delta\bar{\mu}_2 $ ]	S <sub>1</sub>	S <sub>2</sub>
1	415.7	0.147	362.8	0.373	118 → 120 8.9% 119 → 120 89.3%	118 → 120 86.4% 119 → 120 8.4% 119 → 121 2.3%	26.4 [0.0]	27.5 [1.1]	$\pi\pi^*$	$\pi\pi^*$
2	418.4	0.179	356.7	0.167	115 → 120 4.1% 118 → 120 59.8% 119 → 120 33.7%	112 → 120 23.4% 114 → 120 18.3% 115 → 120 39.5%	51.5 [7.2]	45.6 [13.1]	(n/π) $\pi^*$	(n/π) $\pi^*$
3	420.5	0.183	354.2	0.146	111 → 120 4.4% 116 → 120 94.1%	107 → 120 2.6% 111 → 120 36.3% 112 → 120 52.9%	71.8 [68.5]	62.4 [77.8]	$\pi\pi^*$	n $\pi^*$
1'	428.3	0.133	371.3	0.413	138 → 140 10.0% 139 → 140 88.5%	138 → 140 85.4% 139 → 140 9.5% 139 → 141 2.3%	26.4 [0.4]	27.2 [1.2]	$\pi\pi^*$	$\pi\pi^*$
2'	433.0	0.089	364.4	0.243	135 → 140 3.0% 138 → 140 43.2% 139 → 140 52.9%	135 → 140 82.6% 136 → 140 5.1% 138 → 140 4.5%	43.3 [15.0]	44.6 [13.7]	n $\pi^*$	$\pi\pi^*$
2''	430.5	0.167	366.1	0.353	142 → 145 6.0% 144 → 145 92.2%	140 → 145 2.8% 142 → 145 84.8% 144 → 145 5.9%	18.8 [1.3]	19.0 [1.5]	$\pi\pi^*$	$\pi\pi^*$
3'	433.9	0.167	365.0	0.313	131 → 140 5.4% 135 → 140 4.3% 136 → 140 89.1%	128 → 140 3.8% 131 → 140 86.9% 136 → 140 4.2%	—	—	$\pi\pi^*$	$\pi\pi^*$
Exp.	445 <sup>a</sup>		372 <sup>a</sup>				6.1 [1.1] <sup>b</sup>	12.3 [1.6] <sup>b</sup>		

<sup>a</sup> This work. <sup>b</sup> At 66° taken from ref. 83.

yielded an unreliable structure. The energies in kcal mol<sup>-1</sup> relative to the corresponding ground state, of all obtained excited state species, together with the vertical excitation energies are summarised in Table S1 (ESI†). As expected, the lowest-energy excited species are the triplet T<sub>1</sub> followed by the S<sub>1</sub> states. The optimised S<sub>2</sub> states are predicted between 0.8 (2') to 12 (2'') kcal mol<sup>-1</sup> higher in energy than the S<sub>1</sub> ones. Optimisation of the excited states yielded somewhat similar structures with only hydrogen-bond rearrangement in the micro-solvated species. The difference noted above with respect to the S<sub>0</sub> → S<sub>1</sub> excitations of 2' and 2'' was not reflected in their obtained S<sub>1</sub> structures. Geometries, relative energies to S<sub>0</sub> and charge distributions point to similar  $\pi\pi^*$  states for both models. The largest differences in bond lengths between the GS and excited micro-solvated species are collected in Table S2 (ESI†). The major perturbation from the ground state geometry is located in the isoalloxazine ring, around the C<sub>6</sub>, C<sub>7</sub>, C<sub>4a</sub>, and N<sub>5</sub> atoms, and lie in the 2nd decimal place with an average bond increase of ~0.04 Å. Larger differences are found in inter- and intramolecular hydrogen bonds. A shortening of the N<sub>5</sub> ··· H-OH hydrogen bond by ~0.1 Å is evidenced in the 1'–3 excited states, which is in agreement with increased N<sub>5</sub> basicity.<sup>19</sup> The strongest H-bond is predicted in the triplet state in both 2' and 2'' (shortening by 0.10 and 0.13 Å, respectively). This result is in agreement with the increased susceptibility of excited FMN to hydrogen transfer by the conserved cysteine residue in the LOV protein environment. The opposite trend is evidenced for the intramolecular bond at N<sub>1</sub>, which is predicted weaker in the triplet state by 0.04–0.06 Å, with the exception of 2' (–0.07 Å). For symmetrical FMN absorption–emission bands such as those displayed in Fig. 3c, the 0–0 transition (S<sub>1</sub>) can be determined, approximately, by the intersection between the absorption and

fluorescence bands (or the midpoint of the Stokes shift).<sup>84</sup> The 0–0 transition of FMN is determined at 492 nm which is in excellent agreement with the computed values of 494 nm for models 2' and 2'' (Table S3, ESI†).

In order to gain insight on the ISC of FMN, spin–orbit coupling terms were computed for model 2'' and are shown in Table S5 (ESI†). They were determined for the ground state geometry and the two optimised excited states obtained (S<sub>1</sub> and S<sub>2</sub>). Overall, modest couplings are predicted between the singlet and triplet states of FMN with values around ~30–40 cm<sup>-1</sup> for the strongest of those. For comparison, thiobases display SOCs of over 100 cm<sup>-1</sup>,<sup>85</sup> and are known to exhibit ultrafast intersystem crossing within femtoseconds,<sup>79</sup> a result which is consistent with the above. The strongest couplings are expected between singlet–triplet n $\pi^*$  states involving phosphate oxygen lone pairs, and this is maintained for both GS and ES geometries.

To aid the interpretation of the TA results, further excitations to higher states were computed from the T<sub>1</sub> state for all the models studied. These were augmented with real-time TDDFT calculations to the S<sub>1</sub> and S<sub>2</sub> state of 2''. The strongest bands at each of the regions I–V are listed in Table S4 (ESI†). From the experimental findings, intense ESA bands from the low-lying excited singlet state are expected between 500–530 nm (region III) and ~400 nm (region I). Most of the triplet T–T excitations are expected as per the literature,<sup>81</sup> within 600–800 nm (region V).

To link the key TA components (1st, 3rd and 4th) with the calculations, difference absorption spectra of 2'' were devised, as shown in Fig. 5. Each difference spectrum was constructed by combining three of the constituent plots: first, an excited state calculation (RT-TDDFT for S<sub>1</sub> or TDDFT for T<sub>1</sub>) as a positive signal, describing the ESA portion of the spectrum. Second, the ground state absorption S<sub>0</sub> → S<sub>1</sub> band with a

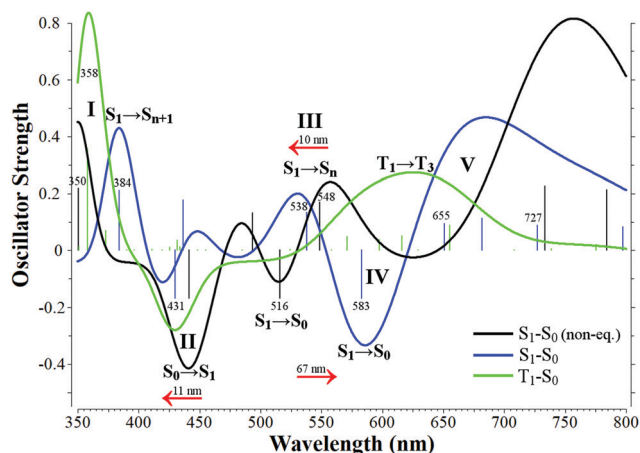


Fig. 5 Calculated difference absorption spectra of model  $2''$ . (i) The black curve, simulates the experimental 1st EAS of Fig. 3c. The excited-state (positive) portion is constructed by a zero-field corrected RT-TDDFT ( $S_1$ ) gradient calculation employing the GS geometry. To form the negative portion of the spectrum, the  $S_0 \rightarrow S_1$  band is subtracted with a non-equilibrium correction (red arrow, 11 nm), together with the fluorescence band (516 nm). (ii) The blue curve, simulating the experimental 3rd EAS, is constructed using the positive signal of the RT-TDDFT  $S_1$  calculation in its optimised geometry. The ground-state  $S_0 \rightarrow S_1$  band (431 nm) is subtracted together with the fluorescence band, which includes a non-equilibrium correction (red arrow, 67 nm). (iii) The green curve, simulating the experimental 4th EAS, includes the TDDFT  $T_1$  state calculation as positive signal while only the ground-state  $S_0 \rightarrow S_1$  band (431 nm) is subtracted. The oscillator strengths and wavelengths of the constituent spectra are shown with sticks of corresponding colour. Labels denote bands of the constituent spectra and transition assignments of the observable bands, and the Latin numerals correspond to the regions of Fig. 3c. The intensities of the difference spectra were multiplied by three with respect to the constituent spectra and a FWHM of 0.12 eV was introduced to ensure distinguishable peaks.

negative sign to simulate the ground-state bleach (GSB). And third, the calculated fluorescence band, also with a negative sign to reproduce the stimulated emission (SE). The fluorescence band was not subtracted from the  $T_1$  plot (green line). The constituent plots are shown in the ESI† with the addition of the  $S_2$  spectrum and the  $S_0$  absorption at the B3LYP-D/6-31G\* level (Fig. S12, ESI†), and their wavelengths and oscillator strengths are represented with sticks in Fig. 5. To ensure comparable intensities between the gas phase and PCM calculations, the ground-state  $S_0 \rightarrow S_1$  band was used as a reference. The intensity of the gas phase band was set to the oscillator strength of the PCM calculation (Table 2,  $f = 0.167$ ) from an original value of  $f = 0.055$  and all other gas phase bands were adjusted accordingly.

In particular, the 3rd component spectrum (blue line) was constructed from a RT-TDDFT calculation of the optimised  $S_1$  structure of  $2''$ . Since a state near the vertical emission is described, the state-specific corrected fluorescence band (583 nm) was subtracted from the above, together with the ground-state absorption spectrum without state-specific correction. It should be noted that the RT-TDDFT spectrum includes both the stimulated emission band at 604 nm and a ground-state bleach signal at 480 nm (Fig. S12, ESI†). Nevertheless, only the positive part of the spectrum was included, while the negative signals were described more fittingly by the PCM calculations. The 2nd component

(black line) was constructed from a RT-TDDFT calculation of  $2''$  using the ground state geometry and computing the gradient for the  $S_1$  excitation including a field-free reference correction. Similarly, only the positive part of the spectrum was included while the GSB and SE bands were simulated by the PCM calculations (Table S4, ESI†). Since this state is close to the vertical excitation, the ground-state absorption spectrum with state-specific correction for the  $S_0 \rightarrow S_1$  band was subtracted, together with the fluorescence band with no state-specific correction (516 nm, Table S3, ESI†). Finally, the 4th component (green) was constructed by combining the absorption spectrum of the  $T_1$  state of  $2''$  obtained by TDDFT and subtracting only the ground state absorption spectrum.

The simulated ESA plots agree well with the features of the regions I–V of the experimental spectra. The ESA band in region III is predicted slightly shifted to 538 nm. The blue-shift of the 511 nm band in region III is reproduced by the non-equilibrium scheme, and the broad intense band in the 4th component (712 nm) is described by computed bands of the  $T_1$  state at 655–775 nm. The non-equilibrium fluorescence shift of 67 nm complies with the apparent shift of the SE band between the 1st and 3rd component. It should be stressed here that the produced non-equilibrium correction to the SE band reports only on solvation affecting the shift, while it is documented that multiple factors such as vibronic coupling to dark  $n\pi^*$  states are contributing.<sup>12,86,87</sup> The real-time TDDFT calculation places the SE band even more to the red, albeit using a more modest basis set in the gas phase.

On the other hand, region V singlet-singlet excitations are predicted more intense by the calculations than the broad band of the 1st to 3rd components. These denote singlet states with energy differences of 34–38 kcal mol<sup>-1</sup> from the  $S_1$  state. The  $S_1 \rightarrow S_2$  transition is not expected in that region, since the computed adiabatic energy difference would place it in the near-IR region for  $2''$  (Table S1, ESI†). Also, in the spectrum simulating the 4th EAS, calculations predict the region I band to blue-shift to 358 nm, and the 512 nm band is absent (region III).

With regards to the computed  $S_2$  state, transitions to higher singlets are expected at 337, 516 and 663 nm (Fig. S12, ESI†), indicating that – provided an adequate population exists –  $S_2$  would register in the global analysis. Unfortunately, time delays below 160 fs, where the signal from  $S_2$  and higher singlet states visible, were dominated by coherent artefacts and could not be analysed.

From the TA findings and the calculations, it is surmised that the first three components are reporting on the  $S_1$  population with the 1st is capturing the solvent response to the excitation. This is corroborated by the increase in intensity of the ESA band at ~500 nm. The last component (4th) reports on triplet formation, with ISC observed as early as ~2 ns, manifest by the appearance of the 712 nm band and the disappearance of the stimulated emission band.

### 3.2. Femtosecond stimulated Raman spectroscopy – calculated Raman spectra

The FSRS spectra were split into high (1700–1100 cm<sup>-1</sup>) and low (150–1050 cm<sup>-1</sup>) frequency regions due to a sharp bend in the background around 1050 cm<sup>-1</sup>, though global analysis was

performed for the whole spectrum. Unless noted otherwise, the following discussion refers to the high-frequency “fingerprint” region.

The normalised FSRS spectra in the high-frequency region are shown in Fig. 6 for the unbuffered sample and Fig. S3 (ESI†) for the two samples containing the H<sub>2</sub>O:MES and H<sub>2</sub>O:Tris buffers. The Raman data mirror the TA findings with five components emerging *via* global analysis. The timescales of the 1st to 3rd components were either fixed to their TA counterparts or set free (Fig. 6b and Table 1). When not fixed, differences of a few tens of picoseconds were noted in the lifetimes of the 2nd component of the unbuffered sample while the H<sub>2</sub>O:Tris sample displayed different lifetimes for all components. Fixing the 3rd EAS to the fluorescence lifetime produced a minor differentiation only in the spectrum of the 4th component, (see Fig. S5b for comparison, ESI†). As per the TA findings, the 0th component is disregarded and the  $\tau_1 = 0.6$  ps component is attributed to the delayed medium response to the optical excitation. The 2nd and

3rd EAS have very similar spectral features, with minor shifts of up to  $\sim 1\text{--}2$  cm<sup>-1</sup>. As commented in the TA section, the former reports on a minor relaxation process and the latter on the fully equilibrated S<sub>1</sub> state.<sup>12</sup> By comparing the 1st and 3rd components, peaks sensitive to solvent effects were identified. The more pronounced shifts include peaks at 1192 → 1200, 1408 → 1417 and 1495 → 1500 cm<sup>-1</sup>. Finally, the triplet 4th component exhibits shifts on all major peaks, notably the 1250 → 1274, 1384 → 1362, 1417 → 1396, 1500 → 1521 and 1570 → 1622 cm<sup>-1</sup> while in the 1150–1250 cm<sup>-1</sup> region, there is a decrease in intensity of the 1200 peak and shift to 1189 cm<sup>-1</sup>. Normalised plots, for easier comparison, of the 1st to 4th components with the aforementioned peaks labelled are included in Fig. 6c. The intensity of all peaks decreases from EAS 1 → 4 in the unnormalised spectra.

The low-frequency region of the 1st to 3rd components of all samples is dominated by the two peaks at  $\sim 440\text{--}480$  cm<sup>-1</sup>. Overall the unbuffered spectra (Fig. S4(a) (ESI†), pH = 5.9),

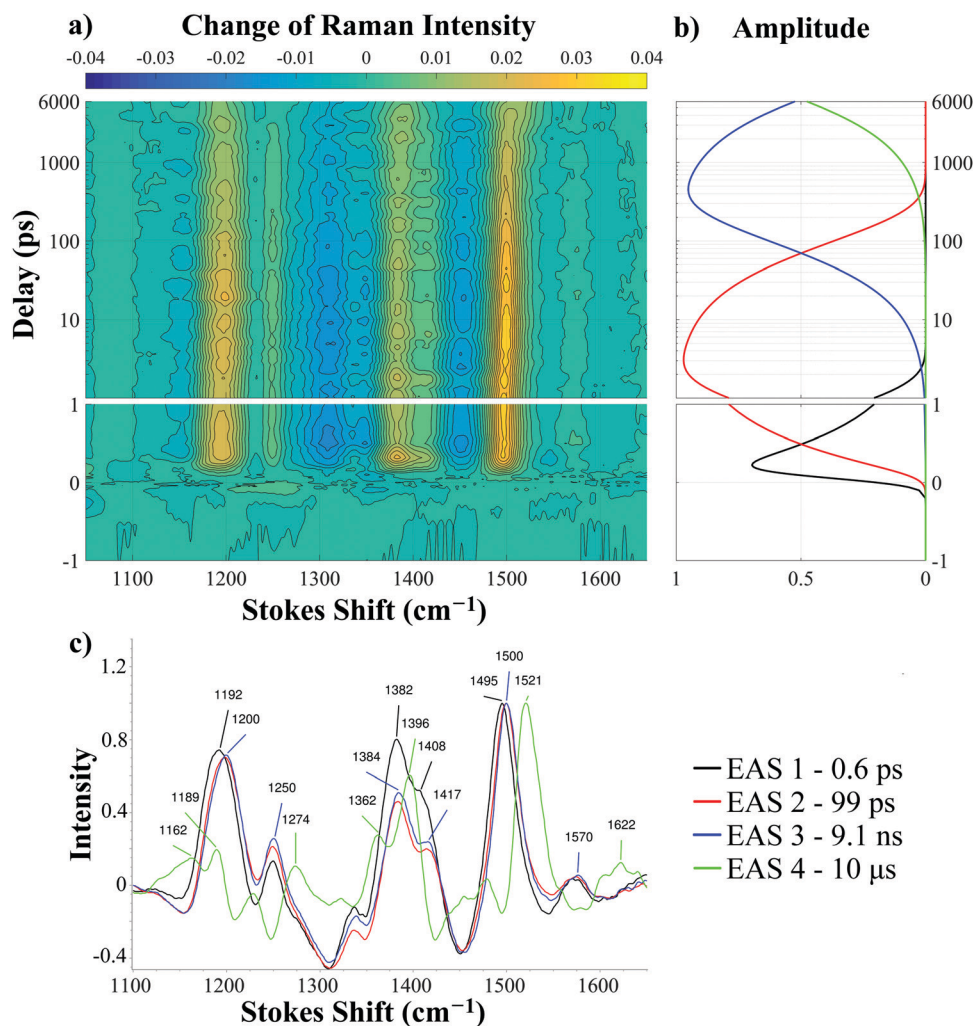


**Fig. 6** Time-resolved femtosecond-stimulated Raman (FSRS) spectra of FMN in the unbuffered water sample with 800 nm Raman pump. (a) Contour plot of the Stokes FSRS spectra at different time delays after 400 nm photoexcitation. (b) Amplitudes from global fitting using a sequential kinetic scheme showing four Raman components with lifetimes  $\tau_1 = 0.6$  ps (black),  $\tau_2 = 99$  ps (red),  $\tau_3 = 9.1$  ns (blue), and the  $\tau_4 = 10$   $\mu$ s component (green). In (a) and (b) the time scale is linear up to 1 ps and logarithmic thereafter. (c) Normalised evolution-associated spectra (EAS) of the latter four components.

H<sub>2</sub>O:MES (Fig. S4(b) (ESI<sup>†</sup>), pH = 6) and H<sub>2</sub>O:Tris (Fig. S4(c) (ESI<sup>†</sup>), pH = 8) appear almost identical. The 4th EAS did not produce workable data in the low-frequency region.

In order to interpret the FSRS-derived EAS, Raman frequency calculations were performed for all the obtained excited-state species (Fig. S13–S16, ESI<sup>†</sup>). To reflect the division of the experimental spectra in high (1100–1750 cm<sup>-1</sup>) and low (100–1050 cm<sup>-1</sup>) frequency regions, the theoretical spectra are also divided in the same high and low regions. For the ground-state calculations, these are shown in Fig. S13a and b (ESI<sup>†</sup>), respectively. The ground-state low-frequency spectra look remarkably similar with shifts of a few cm<sup>-1</sup> between charged and neutral species, making the distinction between them difficult. The only possible marker is a peak at ~927 cm<sup>-1</sup> present in both the GS and S<sub>1</sub> spectrum of **3**, which is due to a symmetric stretching mode of the resonant [-PO<sub>3</sub>]<sup>2-</sup> structure. The experimental H<sub>2</sub>O:MES and H<sub>2</sub>O:Tris spectra exhibit negative peaks to the blue of the computed mode, at 939 and 967 cm<sup>-1</sup>, and positive at 993 and 996 cm<sup>-1</sup>, respectively, which are not present in the unbuffered sample (Fig. S4, ESI<sup>†</sup>). Overall, the low-frequency region contains features of much less intensity than the fingerprint region, associated with modes of lower polarizability. This is supported by the calculations which also predict peaks in the low-frequency region at least one order of magnitude less intense. For further discussion of the computed Raman spectra of the S<sub>0</sub> and S<sub>2</sub> states, see Section S4 of the ESI<sup>†</sup>.

The lowest excited singlet-state (S<sub>1</sub>) Raman spectra are shown in Fig. S15 (ESI<sup>†</sup>). A S<sub>1</sub> structure of **3'** was not obtained, so the spectrum without explicit solvent is included (**3**). Some of the most striking spectral features are included in the 1580–1630 cm<sup>-1</sup> region. These modes are commonly comprised of C<sub>2</sub>=O<sub>2</sub>/C<sub>4</sub>=O<sub>4</sub>' stretching coupled to explicit solvent scissoring and isoalloxazine breathing modes. The most intense peak(s) appear at 1602 cm<sup>-1</sup> in **1'** and 1581 cm<sup>-1</sup> in **2'** (Fig. 9, top right). Labelling the micro-solvated models with D<sub>2</sub>O to decouple these modes from the solvent did not produce a substantial shift. In the absence of explicit solvent, they are predicted to be equally intense at a constant frequency (1589 and 1581 cm<sup>-1</sup> in **1** and **3**, respectively). Only in model **2** the ring breathing is completely decoupled from other modes at 1536 cm<sup>-1</sup>, while the C=O stretches are predicted

less intense at 1590 and 1616 cm<sup>-1</sup>. The bands in the 1100–1300 cm<sup>-1</sup> region are comprised of ring breathing, CH<sub>3</sub> symmetric/asymmetric and ribityl bending modes. The two intense peaks at 1285 and 1299 cm<sup>-1</sup> of **1'** are a mix of ring breathing and C–H in-plane bending modes. For **2'** these are predicted to be less intense at 1284 cm<sup>-1</sup> (medium, m) and 1296 cm<sup>-1</sup> (very weak, vw). Most intense are the 1194 cm<sup>-1</sup> and 1205 cm<sup>-1</sup> peaks involving sugar bending modes. For **3** the most intense Raman band in the region (1177 cm<sup>-1</sup>) is due to C<sub>6,9</sub>-H in-plane bending. The three most intense peak assignments of the S<sub>1</sub> state of **2'** are illustrated in Fig. 9 (top) along with their displacement vectors.

Subsequently, the S<sub>1</sub> spectra of the models **1'**, **2'** and **3** were correlated with the 3rd EAS producing six matched theoretical/experimental pairs (ν<sub>E1</sub>–ν<sub>E6</sub>, Table 3). The constituent modes for each vibration in Table 3 are given in order of decreasing displacement and are made with respect to model **1'**. A plus (+) sign signifies an additional mode and a minus sign (–) one less mode, with respect to **1'**; this notation is kept for all the assignment tables. While their intensities vary, the model **2''** modes are identical to **2'** and are interchangeable. For each of the experimental peaks, only the most intense calculated peaks are included in the correlation, although numerous other vibrations are contributing to their shape. Overall, a good agreement was found between the experimental and theoretical calculations (see Table S6, ESI<sup>†</sup>). Correlation of **2'** with the 3rd EAS revealed an overall mean absolute deviation (MAD) of 32 cm<sup>-1</sup>, and 30 cm<sup>-1</sup> over the three most intense peaks. The biggest discrepancy is caused by the 1581 cm<sup>-1</sup> peak discussed above, which was assigned to the 1500 cm<sup>-1</sup> experimental peak. Alternatively, ν<sub>E2</sub> can be assigned to the predicted 1475 cm<sup>-1</sup> peak of medium (**2'**) and strong intensity (**2''**) which is not assigned to another experimental peak. This is a complex mode involving most of the functional groups of FMN including isoalloxazine bond stretching. Then the agreement is improved to MAD values of 19 cm<sup>-1</sup> overall and 12 cm<sup>-1</sup> over the three most intense peaks. A poorer match was found for the neutral **1'** (48 cm<sup>-1</sup> overall, 47 cm<sup>-1</sup> over intense peaks) and **3'** models (22 cm<sup>-1</sup> overall, 23 cm<sup>-1</sup> over intense peaks). The S<sub>2</sub> spectra do not correlate well with the 3rd EAS, with over 30 cm<sup>-1</sup> of

**Table 3** Correlation between the excited-state Raman spectra (9.1 ns, 3rd component) and the calculated spectra of the singlet excited S<sub>1</sub> state of **1'**, **2'** (**2''**) and **3**

ν	Experimental			Calculated			FMN Modes		
	H <sub>2</sub> O	H <sub>2</sub> O:MES	H <sub>2</sub> O:Tris	<b>1'</b>	<b>2'/2''</b>	<b>3</b>	<b>1'</b>	<b>2'/2''</b>	<b>3</b>
ν <sub>E1</sub>	1570 w	1584 br, w	1578 w	1614 w	1623 m	1616 m	scH <sub>2</sub> O, rN <sub>3</sub> -H	<b>1'</b> + sC <sub>2</sub> =O <sub>2</sub> '	<b>1'</b> - scH <sub>2</sub> O, sC <sub>2</sub> =O <sub>2</sub> ', sC <sub>4</sub> =O <sub>4</sub> '
ν <sub>E2</sub>	1500 vs	1499 vs	1500 vs	1602 s	1581 vs	1581 vs	scH <sub>2</sub> O, rN <sub>3</sub> -H, sC <sub>2</sub> =O <sub>2</sub> ' rN <sub>3</sub> -H, scC <sub>11</sub> H <sub>2</sub> , arCH <sub>3</sub> , sN <sub>1</sub> -C <sub>10a</sub> , sC <sub>4</sub> -C <sub>4a</sub> , sC <sub>7</sub> -C <sub>8</sub> , sC <sub>6</sub> -C <sub>5a</sub>	<b>1'</b> - rN <sub>3</sub> -H + sC <sub>4</sub> =O <sub>4</sub> ' rC <sub>6,9</sub> -H + <b>1'</b> - scC <sub>11</sub> H <sub>2</sub>	rC <sub>6,9</sub> -H, sC <sub>8</sub> -C <sub>9</sub> , sC <sub>6</sub> -C <sub>5a</sub> <b>1</b> + rC <sub>9</sub> -H
ν <sub>E3</sub>	1417 s	1417 m	1417 m	1403 s	1402 s	1401 m	tC <sub>11</sub> H <sub>2</sub> , rC <sub>12,13</sub> -H, arCH <sub>3</sub>	sN <sub>5</sub> -C <sub>4a</sub> , sC <sub>6</sub> -C <sub>5a</sub>	rC <sub>12,13,14</sub> -H, rO <sub>14</sub> '-H
ν <sub>E4</sub>	1384 s	1380 s	1385 s	1382 m	1379 m	1373 s	tC <sub>11</sub> H <sub>2</sub> , rC <sub>12,13,14</sub> -H	tC <sub>11</sub> H <sub>2</sub> , rC <sub>13</sub> -H, srCH <sub>3</sub>	<b>2'</b> - rC <sub>13</sub> -H
ν <sub>E5</sub>	1250 w	1250 m	1251 m	1354 m	1284 w	1260 m	srCH <sub>3</sub> , rC <sub>6</sub> -H	rC <sub>6,9</sub> -H	rC <sub>12,13</sub> -H
ν <sub>E6</sub>	1200 s	1196 s	1202 s	1299 vs	1205 s	1177 s	tC <sub>11</sub> H <sub>2</sub> , rC <sub>14</sub> -H	rC <sub>12,13</sub> -H, rO <sub>12',13'</sub> -H, tC <sub>11</sub> H <sub>2</sub>	rC <sub>6,9</sub> -H, sC <sub>2</sub> -N <sub>3</sub> , sC <sub>4</sub> -C <sub>4a</sub>
				1285 s			rC <sub>6,9</sub> -H		

Intensities vs: very strong, s: strong, m: medium, w: weak, vw: very weak br: broad. Assignments: s – stretch, a – antisymmetric, s – symmetric, w – wag, t – twist, sc – scissor, r – rock.

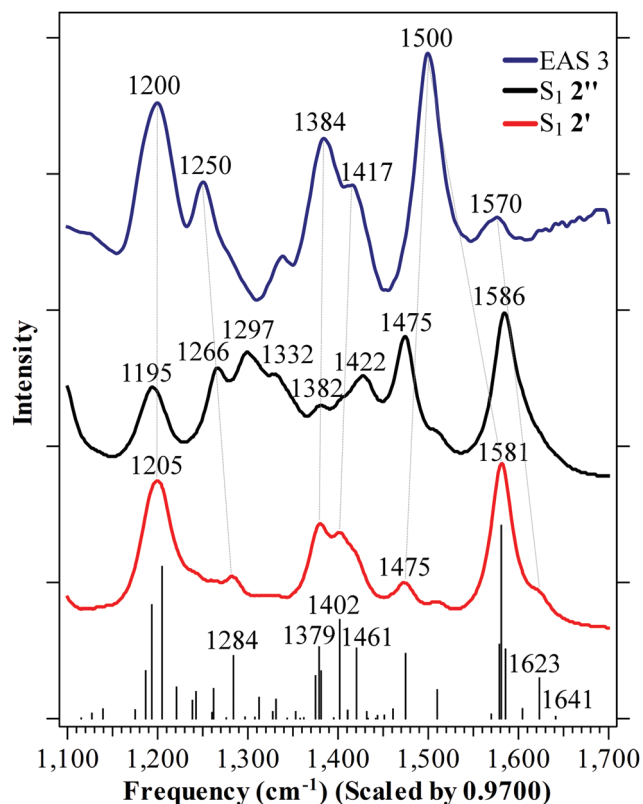


Fig. 7 Comparison between the calculated  $S_1$  Raman spectra of  $2'$  (red) and  $2''$  (black) and the 3rd component (repeated here from Fig. 6c, blue line) in the high-frequency region. All assigned peaks from Table 2 are labelled. Correlated excited-state peaks are indicated with a grey dotted line.

deviation for all models. Apart from the MAD values, the intensities of the experimental peaks matched qualitatively the  $S_1$  state calculations and provided confidence to the attempted theoretical-experimental correlations. Thus, no trace of  $S_2$  state was found, as was surmised by the TA findings. The Raman spectra of  $2'$  and  $2''$  in combination with the 3rd component FSRS are shown in Fig. 7 and the assignments based on Table 3 are indicated with dotted grey lines. With regards to intensities, the spectrum of  $2'$  offers superior agreement in the region  $1382$ – $1475$   $\text{cm}^{-1}$  than  $2''$ .

For the calculations pertaining the  $T_1$  state, all the Raman spectra are collected in Fig. S16 (ESI $\dagger$ ). The computed intensities did not afford a straightforward correlation with the 4th component, hinting at a degree of resonance. Since the Raman pump wavelength at  $800$  nm is close to the triplet-triplet transitions of FMN, the pre-resonance conditions should be included. To calculate theoretical pre-resonance spectra, the  $712$  nm band of the long component was chosen as the reference T-T transition ( $T_{\text{exp}}$ ). Then the incident light wavelength for the calculation ( $I_{\text{calc}}$ ) can be determined by eqn (1), where  $I_{\text{exp}}$  is the wavelength of the Raman pump of the experiment, and  $T_{\text{calc}}$  is the chosen theoretical T-T transition:

$$I_{\text{calc}} = T_{\text{calc}} + (I_{\text{exp}} - T_{\text{exp}}) \quad (1)$$

Several T-T transitions were predicted by the calculations in the region around  $\sim 800$  nm, and for each of those, a different

incident light is specified by eqn (1). These are collected in Table S7 (ESI $\dagger$ ) for  $2'$  and  $2''$ . For  $2'$  three T-T transitions ( $T_{\text{calc}}$ ) were chosen based on their intensity and proximity to  $T_{\text{exp}}$ , namely at  $657$ ,  $830$ , and  $706$  nm, given in order of decreasing oscillator strength. Similarly, for  $2''$  four transitions were determined at  $655$ ,  $775$ ,  $739$  and  $708$  nm. For instance, to determine the incident light frequency of the T-T transition at  $775$  nm,  $T_{\text{calc}}$  is set to  $775$ ,  $I_{\text{exp}} = 800$  and  $T_{\text{exp}} = 712$ . Then eqn (1) gives an  $I_{\text{calc}}$  value of  $863$  nm, which translates to a Raman incident light frequency of  $11\,588$   $\text{cm}^{-1}$  (see also Table S7 and Fig. S17, S18 (ESI $\dagger$ ) for the rest of the  $I_{\text{calc}}$  values).

For the two bands at  $1528$  and  $1542$   $\text{cm}^{-1}$  the calculations of  $2'$  predict diminishing intensities with each decrease of the incident light wavelength (Fig. S17, ESI $\dagger$ ), while the  $1391$   $\text{cm}^{-1}$  is predicted as the most intense peak when pre-resonant to the  $830$  nm T-T band (orbitals and their coefficients of  $T_{830}$  are included in Fig. S11a, ESI $\dagger$ ). Conversely, for  $2''$  the bands below  $1300$   $\text{cm}^{-1}$  are predicted less intense with increasing  $I_{\text{calc}}$  and the peaks at  $1389$  and  $1511$   $\text{cm}^{-1}$  emerge as the most intense in the spectrum (Fig. S18, ESI $\dagger$ ).

For the correlation with the experimental 4th EAS, the pre-resonance spectrum belonging to the  $775$  nm T-T transition of  $2''$  was chosen ( $T_{775}$ , black line, Fig. 8). The  $739$  nm transition could also be selected (Fig. S18, ESI $\dagger$ ) being closer to the  $T_{\text{exp}}$  at  $712$  nm, but it is predicted with a much lower oscillator strength. Nevertheless, both these transitions provide spectra with very similar intensities (only the nature of the transition changes). The orbitals involved in the  $775$  nm T-T transition

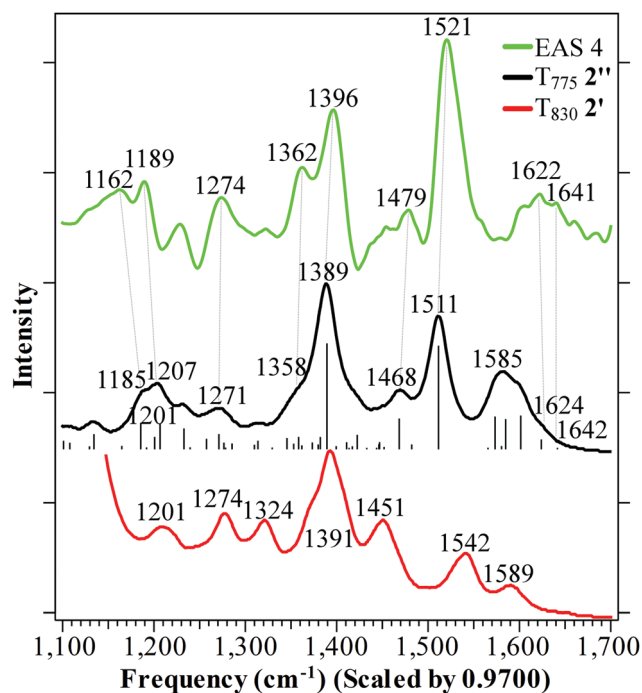


Fig. 8 Comparison between the calculated triplet pre-resonant Raman spectra of models  $2'$  ( $T_{830}$ , red line),  $2''$  ( $T_{775}$ , black line) and the FSRS 4th component (repeated here from Fig. 6c, green line) in the high-frequency region. All assigned peaks from Table 4 are labelled. Correlated excited-state peaks are indicated with a grey dotted line.

**Table 4** Correlation between the excited-state Raman spectra of the 4th component and the calculated spectra for the  $T_1$  state of  $2'$  and  $2''$ . The correlation was made possible with the re-computed intensities of the 775 nm T–T transition of  $2''$

$\nu$	Experimental	Calculated		FMN modes	
	H <sub>2</sub> O	$2'$	$2''$	$2'$	$2''$
$\nu_{T1}$	1641 vw	1646 vw	1642 vw	scH <sub>2</sub> O, rN <sub>3</sub> -H	scH <sub>2</sub> O, rN <sub>3</sub> -H
$\nu_{T2}$	1622 w, br	1602 vw	1624 m	scH <sub>2</sub> O, sC <sub>4</sub> =O <sub>4'</sub> , rN <sub>3</sub> -H	scH <sub>2</sub> O, rN <sub>3</sub> -H, sC <sub>2</sub> =O <sub>2'</sub>
$\nu_{T3}$	1521 vs	1542 s	1511 vs	rN <sub>3</sub> -H, sC <sub>2</sub> =O <sub>2'</sub> , sC <sub>4</sub> =O <sub>4'</sub> , sC <sub>8</sub> -C <sub>7</sub> , sC <sub>9a</sub> -C <sub>5a</sub> , sC <sub>10a</sub> -C <sub>4a</sub>	sN <sub>1</sub> -C <sub>10a</sub> , sC <sub>4</sub> -C <sub>4a</sub> , rN <sub>3</sub> -H, rC <sub>9</sub> -H
$\nu_{T4}$	1479 vw	1451 s	1468 s	scC <sub>15</sub> H <sub>2</sub>	scC <sub>11</sub> H <sub>2</sub> , arCH <sub>3</sub>
$\nu_{T5}$	1396 s	1391 vs	1389 vs	scC <sub>11</sub> H <sub>2</sub> , rC <sub>12,13,14</sub> -H, rO <sub>13',14'</sub> -H	tC <sub>11</sub> H <sub>2</sub> , rC <sub>12,14</sub> -H, rC <sub>6</sub> -H
$\nu_{T6}$	1362 m	1371 s	1358 m	tC <sub>15</sub> H <sub>2</sub>	scC <sub>11,15</sub> H <sub>2</sub> , rC <sub>12,14</sub> -H, rO <sub>12',13'</sub> -H, rC <sub>9</sub> -H
$\nu_{T7}$	1274 vw	1274 s	1271 m	rC <sub>12,13,14</sub> -H	rC <sub>12,13,14</sub> -H
$\nu_{T8}$	1189 w	1201 m	1207 s	rC <sub>13</sub> -H, rO <sub>13'</sub> -H	rC <sub>12,13,14,15</sub> -H, rO <sub>12',13'</sub> -H
$\nu_{T9}$	1162 w	1183 w	1185 s	rC <sub>6,9</sub> -H, tC <sub>11</sub> H <sub>2</sub> , rC <sub>12</sub> -H, rO <sub>12'</sub> -H	rC <sub>6,9</sub> -H, tC <sub>11</sub> H <sub>2</sub> , rC <sub>12</sub> -H, rO <sub>12'</sub> -H

Intensities (based on pre-resonance calculations) vs: very strong, s: strong, m: medium, w: weak, vw: very weak br: broad. Assignments: s – stretch, a – antisymmetric, s – symmetric, w – wag, t – twist, sc – scissor, r – rock.

are shown in Fig. S11b (ESI<sup>†</sup>) along with their coefficients. Orbitals 140–141 with the highest contribution are localised mostly in the ribityl and phosphate moieties determining  $T_{775}$  as a  $n\pi^*$  state, involving phosphate oxygen lone pairs. The  $T_{775}$  state is similar to  $T_8$  (Table S5, ESI<sup>†</sup>) which is predicted with the highest spin–orbit coupling term to the equivalent singlet ( $T_7'$  and  $T_7''$  for  $S_1$  and  $S_2$  geometries, respectively). From the spin density surface it is surmised that the triplet unpaired electrons are localised in the isoalloxazine ring (see also discussion in the ESI<sup>†</sup>). With the re-computed Raman intensities, correlation with experiment was made more facile, and excellent agreement was achieved with an overall MAD of 9  $\text{cm}^{-1}$  ( $\nu_{T1}$ – $\nu_{T9}$  pairs, Table 4). The  $\nu_{T5} = 1389$  [1396]  $\text{cm}^{-1}$  and  $\nu_{T3} = 1511$  [1521]  $\text{cm}^{-1}$  pairs that are enhanced due to (pre)resonance (assigned 4th EAS peaks in brackets), are attributed to complex normal modes (Fig. 9, bottom).

Since adequate experimental–theoretical correlation was achieved, an attempt to rationalise the peak shifts observed among the key components can be made. Blue-shifts between

the 1st and 3rd components are expected to originate in vibrational modes involving solvent-sensitive functional groups ( $\nu_{E2}$ ,  $\nu_{E3}$ ,  $\nu_{E6}$ ). On the other hand, modes involving C–H bonds ( $\nu_{E4}$ ,  $\nu_{E5}$ ) remain unaffected. The exception to the above is the assigned peak to  $\nu_{E1}$  containing N<sub>3</sub>-H bending and C<sub>2</sub>=O<sub>2'</sub> stretching modes, which is unaffected by solvent equilibration.

With regards to the singlet–triplet shifts, the observed  $\nu_{E2}/\nu_{T3}$  21  $\text{cm}^{-1}$  shift can be explained by the assignment of 1475  $\text{cm}^{-1}$  to  $\nu_{E2}$  providing a calculated 36  $\text{cm}^{-1}$  shift to the equivalent triplet ( $\nu_{T3} = 1511$   $\text{cm}^{-1}$ ). The  $\nu_{E2}/\nu_{T3}$  pair includes isoalloxazine bond stretching modes which are shortened in the triplet state causing the shift to higher frequency. Then the intense peaks at 1581 ( $2'$ ) and 1586 ( $2''$ )  $\text{cm}^{-1}$  can be assigned to the experimental 1570  $\text{cm}^{-1}$  peak which shifts to 1622  $\text{cm}^{-1}$  in the triplet spectrum, even though there is a mismatch in intensities. The assigned peaks 1602 and 1624  $\text{cm}^{-1}$  (for  $2'$  and  $2''$  respectively) involve the C=O bonds which are again shortened in the triplet-state. The above computed shortening of the bonds involved in the normal modes provide the rationale for interpreting all the observed blue-shifts.

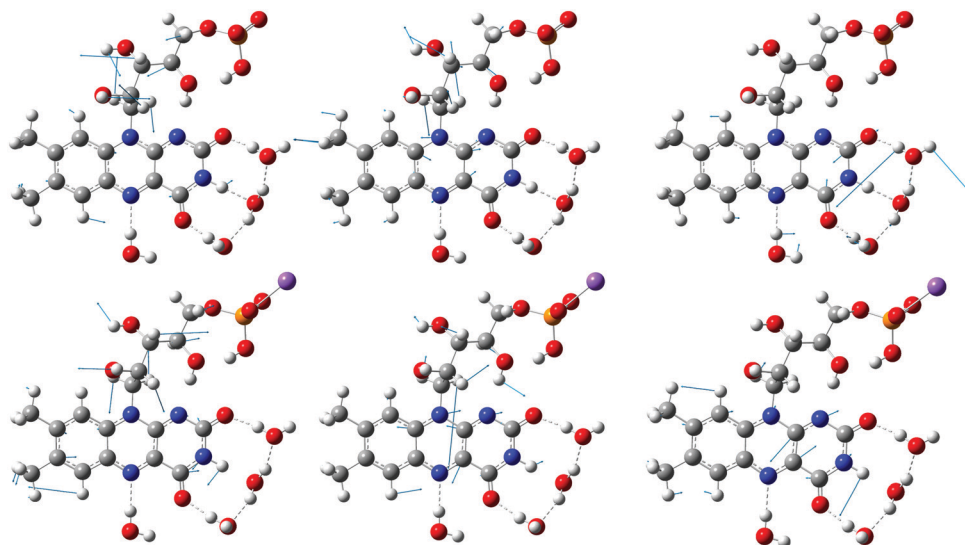


**Fig. 9** Prominent vibrations of the  $S_1$  and  $T_1$  states of  $2'$  and  $2''$ , respectively. The  $S_1$  state vibrations are shown on the top:  $\nu_{E6} = 1205$  [1200]  $\text{cm}^{-1}$  (top, left),  $\nu_{E4} = 1379$  [1384]  $\text{cm}^{-1}$  (top, middle) and  $\nu_{E2} = 1581$  [1500]  $\text{cm}^{-1}$  (top, right). The excited triplet  $T_1$  vibrations are shown on the bottom:  $\nu_{T8} = 1207$  [1189]  $\text{cm}^{-1}$  (bottom, left),  $\nu_{T5} = 1389$  [1396]  $\text{cm}^{-1}$  (bottom, middle) and  $\nu_{T3} = 1511$  [1521]  $\text{cm}^{-1}$  (bottom, right). Values in brackets denote the assigned experimental peaks.

The  $1384 \rightarrow 1362 \text{ cm}^{-1}$  and  $1417 \rightarrow 1396 \text{ cm}^{-1}$  shifts are also reproduced by the assigned  $\nu_{E4}/\nu_{T6}$  and  $\nu_{E3}/\nu_{T5}$  pairs, respectively. In  $2'$  the former pair is assigned to  $1379 \rightarrow 1371 \text{ cm}^{-1}$  and the latter to  $1402 \rightarrow 1391 \text{ cm}^{-1}$ , while in  $2''$  the pairs are  $1379 \rightarrow 1358 \text{ cm}^{-1}$  and  $1403 \rightarrow 1389 \text{ cm}^{-1}$ . Finally, the shift from singlet to triplet of the peak at  $1250 \rightarrow 1274 \text{ cm}^{-1}$  is predicted with opposite sign by the assigned pair  $\nu_{E5}/\nu_{T7}$  ( $1284 \rightarrow 1274 \text{ cm}^{-1}$  ( $2'$ ) and  $1283 \rightarrow 1271 \text{ cm}^{-1}$  ( $2''$ )). An alternative assignment by the  $1266 \text{ cm}^{-1}$  peak of  $2''$  reproduces the shift, but this would leave equally intense peaks at  $1297$  and  $1332 \text{ cm}^{-1}$  unassigned (Fig. 7, black line). All equivalent vibrations found between the  $S_1$  and  $T_1$  states of  $2'$  and  $2''$  are included in Table S8 (ESI<sup>†</sup>). As mentioned above, the  $S_1$  vibrations of  $2'/2''$  are comparable, reflecting similar variations between their respective GS geometries, while Table S8 (ESI<sup>†</sup>) and Fig. 8 demonstrate a larger divergence in the  $T_1$  state. This is reflected in the bottom rows of Table S2 (ESI<sup>†</sup>) where changes in the bond lengths between the  $S_1$  and  $T_1$  states are highlighted.

The intersystem crossing from the lowest excited singlet to the lowest triplet state ( $T_1$ ) was indirectly inferred by the formation of the triplet species (2–3 ns). No intermediate  $n\pi^*$  state was evidenced by either TA or FSRs, while calculations point to an involvement of phosphate oxygen lone pairs in addition to the lone pair  $n\pi^*$  states common to all isoalloxazine systems. The precise mechanism of intersystem crossing in FMN requires further investigation both experimentally and computationally.

## 4. Conclusions

The excitation population of FMN was monitored by transient absorption and, for the first time to the best of our knowledge, by femtosecond stimulated Raman spectroscopy (FSRS). The intersystem crossing (ISC) from the lowest excited singlet to the triplet state was evidenced with both spectroscopies and located well within the experimental time window of 5 ns (6 ns for FSRs). Global analysis revealed a component describing solvent dynamics with a lifetime of 0.6 ps, a long-lived excited singlet state  $S_1$  (>6 ns), and the lowest triplet state  $T_1$  with a lifetime well beyond the experimental time window. The latter was monitored by the appearance of the 712 nm band in the TA, and the blue-shift of the FSRs peak to  $1500 \rightarrow 1521 \text{ cm}^{-1}$  (among others), formed at a 2–3 ns rate, which is an approximate timescale range for the ISC of FMN. Accurate assignments for both TA and Raman spectra were provided by comprehensive quantum chemistry calculations (TDDFT). Two different configurations of FMN were examined with respect to the experimental pH value, one with a negative charge, and one cation-balanced. The difference between the two models was identified as an increase in the  $n\pi^*$  character of  $S_1$  due to the participation of phosphate oxygen lone pairs in the charged model which was attributed to self-interaction error. Moreover, this difference was not present in the optimised species where both models yielded equivalent  $S_1$   $n\pi^*$  states. The negatively charged FMN model provided better qualitative agreement with the  $S_1$  Raman spectrum, while the cation-balanced FMN described more adequately the TA and

Raman triplet spectra. Other models were employed to emulate solutions with pH values higher than the second deprotonation  $pK_a$  of the phosphate moiety. Calculations predicted a unique peak at  $927 \text{ cm}^{-1}$  due to a symmetric stretching mode of the resonant  $[-\text{PO}_3]^{2-}$  structure which was evidenced in the low-frequency region of the  $\text{H}_2\text{O}:\text{MES}$  (pH = 6) and  $\text{H}_2\text{O}:\text{Tris}$  (pH = 8) samples at  $\sim 990 \text{ cm}^{-1}$  but not in the unbuffered sample. No other charge effect was evidenced within the pH range 6–8. Band shifts near the vertical excitations/emissions were rationalised with the inclusion of non-equilibrium corrections to the computed bands. Correlation between the experimental and computed spectra of the long-lived singlet and triplet species yielded MAD values as low as 19 and  $9 \text{ cm}^{-1}$ , respectively. In particular, the triplet Raman spectrum assignment was facilitated by the inclusion of pre-resonance conditions to the computed intensities, attributed to the interaction of the 800 nm Raman pump with the 712 nm T–T band. The chosen  $n\pi^*$  triplet state that gave the best match with the experimental spectrum, was found to have a relatively strong spin–orbit coupling to the equivalent  $n\pi^*$  singlet state, both of which involve lone pairs of the phosphate moiety. A similar joint FSRs/QM approach can be used to track the structural evolution of excited FMN bound to LOV photoreceptors.

## Conflicts of interest

There are no conflicts to declare.

## Acknowledgements

The work was supported by the project Structural dynamics of biomolecular systems (ELIBIO) (CZ.02.1.01/0.0/0.0/15\_003/0000447) and the project Advanced research using high intensity laser produced photons and particles (ADONIS) (CZ.02.1.01/0.0/0.0/16\_019/0000789) from the European Regional Development Fund and the Ministry of Education, Youth and Sports (MEYS) of the Czech Republic. The Institute of Biotechnology of the Czech Academy of Sciences acknowledges the institutional grant RVO 86652036. We also acknowledge CMS-Biocev (“Biophysical techniques”) supported by MEYS CR (LM2015043). The results of the Project LQ1606 were obtained with financial support of MEYS as part of targeted support from the National Programme of Sustainability II. Computational resources were supplied by the project “e-Infrastruktura CZ” (e-INFRA LM2018140) provided within the program Projects of Large Research, Development and Innovations Infrastructures. Computational resources were also provided by the ELIXIR-CZ project (LM2015047), part of the international ELIXIR infrastructure. J. A. acknowledges support from Chalmers Area of Advance; Material Science. P. C. A. and B. S. would like to thank Michal Strand for invaluable IT support.

## References

- 1 S. Weber and E. E. Schleicher, *Flavins and Flavoproteins Methods and Protocols*, 2014.
- 2 A. Losi and W. Gartner, *Photochem. Photobiol.*, 2017, **93**, 141–158.

- 3 T. Fujisawa and S. Masuda, *Biophys. Rev.*, 2018, **10**, 327–337.
- 4 Q. Wang, Z. Zuo, X. Wang, Q. Liu, L. Gu, Y. Oka and C. Lin, *Curr. Opin. Plant Biol.*, 2018, **45**, 120–126.
- 5 A. Losi, K. H. Gardner and A. Moglich, *Chem. Rev.*, 2018, **118**, 10659–10709.
- 6 B. Karasulu and W. Thiel, *J. Phys. Chem. B*, 2015, **119**, 928–943.
- 7 B. Karasulu, J. P. Gotze and W. Thiel, *J. Chem. Theory Comput.*, 2014, **10**, 5549–5566.
- 8 B. Rieff, S. Bauer, G. Mathias and P. Tavan, *J. Phys. Chem. B*, 2011, **115**, 2117–2123.
- 9 B. Klaumunzer, D. Kroner, H. Lischka and P. Saalfrank, *Phys. Chem. Chem. Phys.*, 2012, **14**, 8693–8702.
- 10 R. K. Kar, V. A. Borin, Y. Ding, J. Matysik and I. Schapiro, *Photochem. Photobiol.*, 2019, **95**, 662–674.
- 11 E. Sikorska, I. Khmelinskii, A. Komasa, J. Koput, L. F. V. Ferreira, J. R. Herance, J. L. Bourdelande, S. L. Williams, D. R. Worrall, M. Insińska-Rak and M. Sikorski, *Chem. Phys.*, 2005, **314**, 239–247.
- 12 A. Weigel, A. Dobryakov, B. Klaumunzer, M. Sajadi, P. Saalfrank and N. P. Ernstring, *J. Phys. Chem. B*, 2011, **115**, 3656–3680.
- 13 L. Valle, F. E. Vieyra and C. D. Borsarelli, *Photochem. Photobiol. Sci.*, 2012, **11**, 1051–1061.
- 14 M. Spexard, D. Immeln, C. Thöing and T. Kottke, *Vib. Spectrosc.*, 2011, **57**, 282–287.
- 15 J. Galban, I. Sanz-Vicente, J. Navarro and S. de Marcos, *Methods Appl. Fluoresc.*, 2016, **4**, 042005.
- 16 J. Langer, A. Gunther, S. Seidenbecher, G. Berden, J. Oomens and O. Dopfer, *ChemPhysChem*, 2014, **15**, 2550–2562.
- 17 A. Sengupta, R. V. Khade and P. Hazra, *J. Photochem. Photobiol., A*, 2011, **221**, 105–112.
- 18 S. Salzmann, V. Martinez-Junza, B. Zorn, S. E. Braslavsky, M. Mansurova, C. M. Marian and W. Gartner, *J. Phys. Chem. A*, 2009, **113**, 9365–9375.
- 19 G. Li and K. D. Glusac, *J. Phys. Chem. A*, 2008, **112**, 4573–4583.
- 20 G. Li and K. D. Glusac, *J. Phys. Chem. B*, 2009, **113**, 9059–9061.
- 21 J. N. Iuliano, A. A. Gil, S. P. Laptanok, C. R. Hall, J. Tolentino Collado, A. Lukacs, S. A. Hag Ahmed, J. Abyad, T. Daryae, G. M. Greetham, I. V. Sazanovich, B. Illarionov, A. Bacher, M. Fischer, M. Towrie, J. B. French, S. R. Meech and P. J. Tonge, *Biochemistry*, 2018, **57**, 620–630.
- 22 T. Domratheva, E. Hartmann, I. Schlichting and T. Kottke, *Sci. Rep.*, 2016, **6**, 22669.
- 23 J. N. Iuliano, J. B. French and P. J. Tonge, *Methods Enzymol.*, 2019, **620**, 189–214.
- 24 D. R. Dietze and R. A. Mathies, *ChemPhysChem*, 2016, **17**, 1224–1251.
- 25 P. Kukura, D. W. McCamant and R. A. Mathies, *Annu. Rev. Phys. Chem.*, 2007, **58**, 461–488.
- 26 M. Kloz, R. van Grondelle and J. T. Kennis, *Phys. Chem. Chem. Phys.*, 2011, **13**, 18123–18133.
- 27 M. Kloz, J. Weissenborn, T. Polivka, H. A. Frank and J. T. Kennis, *Phys. Chem. Chem. Phys.*, 2016, **18**, 14619–14628.
- 28 M. Creelman, M. Kumauchi, W. D. Hoff and R. A. Mathies, *J. Phys. Chem. B*, 2014, **118**, 659–667.
- 29 D. W. McCamant, P. Kukura and R. A. Mathies, *J. Phys. Chem. B*, 2005, **109**, 10449–10457.
- 30 M. A. Taylor, L. Zhu, N. D. Rozanov, K. T. Stout, C. Chen and C. Fang, *Phys. Chem. Chem. Phys.*, 2019, **21**, 9728–9739.
- 31 S. Y. Lee, D. Zhang, D. W. McCamant, P. Kukura and R. A. Mathies, *J. Chem. Phys.*, 2004, **121**, 3632–3642.
- 32 D. W. McCamant, P. Kukura and R. A. Mathies, *J. Phys. Chem. A*, 2003, **107**, 8208–8214.
- 33 C. R. Hall, I. A. Heisler, G. A. Jones, J. E. Frost, A. A. Gil, P. J. Tonge and S. R. Meech, *Chem. Phys. Lett.*, 2017, **683**, 365–369.
- 34 P. Drössler, W. Holzer, A. Penzkofer and P. Hegemann, *Chem. Phys.*, 2002, **282**, 429–439.
- 35 S. D. M. Islam, A. Penzkofer and P. Hegemann, *Chem. Phys.*, 2003, **291**, 97–114.
- 36 W. Holzer, A. Penzkofer, M. Fuhrmann and P. Hegemann, *Photochem. Photobiol.*, 2007, **75**, 479–487.
- 37 T. Climent, R. Gonzalez-Luque, M. Merchan and L. Serrano-Andres, *J. Phys. Chem. A*, 2006, **110**, 13584–13590.
- 38 I. H. van Stokkum, M. Gauden, S. Crosson, R. van Grondelle, K. Moffat and J. T. Kennis, *Photochem. Photobiol.*, 2011, **87**, 534–541.
- 39 J. N. Chacon, J. McLearn and R. S. Sinclair, *Photochem. Photobiol.*, 1988, **47**, 647–656.
- 40 A. Losi, E. Polverini, B. Quest and W. Gärtner, *Biophys. J.*, 2002, **82**, 2627–2634.
- 41 J. Zhu, T. Mathes, Y. Hontani, M. T. Alexandre, K. C. Toh, P. Hegemann and J. T. Kennis, *J. Phys. Chem. Lett.*, 2016, **7**, 4380–4384.
- 42 R. J. Kutta, K. Magerl, U. Kensy and B. Dick, *Photochem. Photobiol. Sci.*, 2015, **14**, 288–299.
- 43 K. Lanzl, M. V. Sanden-Flohe, R. J. Kutta and B. Dick, *Phys. Chem. Chem. Phys.*, 2010, **12**, 6594–6604.
- 44 K. Magerl, I. Stambolic and B. Dick, *Phys. Chem. Chem. Phys.*, 2017, **19**, 10808–10819.
- 45 M. T. Alexandre, T. Domratheva, C. Bonetti, L. J. van Wilderen, R. van Grondelle, M. L. Groot, K. J. Hellingwerf and J. T. Kennis, *Biophys. J.*, 2009, **97**, 227–237.
- 46 M. T. Alexandre, R. van Grondelle, K. J. Hellingwerf, B. Robert and J. T. Kennis, *Phys. Chem. Chem. Phys.*, 2008, **10**, 6693–6702.
- 47 S. L. Tan, J. M. Kan and R. D. Webster, *J. Phys. Chem. B*, 2013, **117**, 13755–13766.
- 48 M. S. Barclay, T. J. Quincy, D. B. Williams-Young, M. Caricato and C. G. Elles, *J. Phys. Chem. A*, 2017, **121**, 7937–7946.
- 49 T. J. Quincy, M. S. Barclay, M. Caricato and C. G. Elles, *J. Phys. Chem. A*, 2018, **122**, 8308–8319.
- 50 M. S. Barclay, M. Caricato and C. G. Elles, *J. Phys. Chem. A*, 2019, **123**(36), 7720–7732.
- 51 J. R. Lakowicz, *Principles of Fluorescence Spectroscopy*, 2006.
- 52 J. J. Snellenburg, S. P. Laptanok, R. Seger, K. M. Mullen and I. H. M. van Stokkum, *J. Stat. Softw.*, 2012, **49**, 1–22.
- 53 J. T. Kennis, S. Crosson, M. Gauden, I. H. van Stokkum, K. Moffat and R. van Grondelle, *Biochemistry*, 2003, **42**, 3385–3392.
- 54 A. I. Nash, R. McNulty, M. E. Shillito, T. E. Swartz, R. A. Bogomolni, H. Luecke and K. H. Gardner, *Proc. Natl. Acad. Sci. U. S. A.*, 2011, **108**, 9449–9454.

- 55 J. Rezac, J. Fanfrlik, D. Salahub and P. Hobza, *J. Chem. Theory Comput.*, 2009, **5**, 1749–1760.
- 56 J. Rezac, *J. Comput. Chem.*, 2016, **37**, 1230–1237.
- 57 H. J. C. Berendsen, J. P. M. Postma, W. F. Vangunsteren, A. Dinola and J. R. Haak, *J. Chem. Phys.*, 1984, **81**, 3684–3690.
- 58 K. Kriz and J. Rezac, *J. Chem. Inf. Model.*, 2019, **59**, 229–235.
- 59 M. J. Frisch, G. W. Trucks, H. B. Schlegel, G. E. Scuseria, M. A. Robb, J. R. Cheeseman, G. Scalmani, V. Barone, G. A. Petersson, H. Nakatsuji, X. Li, M. Caricato, A. V. Marenich, J. Bloino, B. G. Janesko, R. Gomperts, B. Mennucci, H. P. Hratchian, J. V. Ortiz, A. F. Izmaylov, J. L. Sonnenberg, D. Williams-Young, F. Ding, F. Lipparini, F. Egidi, J. Goings, B. Peng, A. Petrone, T. Henderson, D. Ranasinghe, V. G. Zakrzewski, J. Gao, N. Rega, G. Zheng, W. Liang, M. Hada, M. Ehara, K. Toyota, R. Fukuda, J. Hasegawa, M. Ishida, T. Nakajima, Y. Honda, O. Kitao, H. Nakai, T. Vreven, K. Throssell, J. A. Montgomery, Jr., J. E. Peralta, F. Ogliaro, M. J. Bearpark, J. J. Heyd, E. N. Brothers, K. N. Kudin, V. N. Staroverov, T. A. Keith, R. Kobayashi, J. Normand, K. Raghavachari, A. P. Rendell, J. C. Burant, S. S. Iyengar, J. Tomasi, M. Cossi, J. M. Millam, M. Klene, C. Adamo, R. Cammi, J. W. Ochterski, R. L. Martin, K. Morokuma, O. Farkas, J. B. Foresman and D. J. Fox, Gaussian, Inc., Wallingford, CT, 2016.
- 60 A. D. Becke, *Phys. Rev. A: At., Mol., Opt. Phys.*, 1988, **38**, 3098–3100.
- 61 C. Lee, W. Yang and R. G. Parr, *Phys. Rev. B: Condens. Matter Mater. Phys.*, 1988, **37**, 785–789.
- 62 F. Weigend and R. Ahlrichs, *Phys. Chem. Chem. Phys.*, 2005, **7**, 3297–3305.
- 63 F. Weigend, *Phys. Chem. Chem. Phys.*, 2006, **8**, 1057–1065.
- 64 S. Grimme, S. Ehrlich and L. Goerigk, *J. Comput. Chem.*, 2011, **32**, 1456–1465.
- 65 J. Tomasi, B. Mennucci and R. Cammi, *Chem. Rev.*, 2005, **105**, 2999–3093.
- 66 G. Scalmani and M. J. Frisch, *J. Chem. Phys.*, 2010, **132**, 114110.
- 67 M. Cossi, V. Barone, R. Cammi and J. Tomasi, *Chem. Phys. Lett.*, 1996, **255**, 327–335.
- 68 G. Scalmani, M. J. Frisch, B. Mennucci, J. Tomasi, R. Cammi and V. Barone, *J. Chem. Phys.*, 2006, **124**, 94107.
- 69 R. Improta, G. Scalmani, M. J. Frisch and V. Barone, *J. Chem. Phys.*, 2007, **127**, 074504.
- 70 R. Improta, V. Barone, G. Scalmani and M. J. Frisch, *J. Chem. Phys.*, 2006, **125**, 054103.
- 71 F. Furche and R. Ahlrichs, *J. Chem. Phys.*, 2002, **117**, 7433–7447.
- 72 J. Liu and W. Liang, *J. Chem. Phys.*, 2011, **135**, 184111.
- 73 J. Liu and W. Liang, *J. Chem. Phys.*, 2011, **135**, 014113.
- 74 P. Pulay, *J. Chem. Phys.*, 1983, **78**, 5043–5051.
- 75 C. E. Dykstra and P. G. Jasien, *Chem. Phys. Lett.*, 1984, **109**, 388–393.
- 76 M. K. Kesharwani, B. Brauer and J. M. Martin, *J. Phys. Chem. A*, 2015, **119**, 1701–1714.
- 77 S. A. Fischer, C. J. Cramer and N. Govind, *J. Chem. Theory Comput.*, 2015, **11**, 4294–4303.
- 78 M. Valiev, E. J. Bylaska, N. Govind, K. Kowalski, T. P. Straatsma, H. J. J. Van Dam, D. Wang, J. Nieplocha, E. Apra, T. L. Windus and W. A. de Jong, *Comput. Phys. Commun.*, 2010, **181**, 1477–1489.
- 79 X. Gao, S. Bai, D. Fazzi, T. Niehaus, M. Barbatti and W. Thiel, *J. Chem. Theory Comput.*, 2017, **13**, 515–524.
- 80 S. G. Chiodo and M. Leopoldini, *Comput. Phys. Commun.*, 2014, **185**, 676–683.
- 81 T. Bernt Melø, M. Adriana Ionescu, G. W. Haggquist and K. Razi Naqvi, *Spectrochim. Acta, Part A*, 1999, **55**, 2299–2307.
- 82 B. Schneider and M. Kabelac, *J. Am. Chem. Soc.*, 1998, **120**, 161–165.
- 83 R. J. Stanley and H. Jang, *J. Phys. Chem. A*, 1999, **103**, 8976–8984.
- 84 C. Adamo and D. Jacquemin, *Chem. Soc. Rev.*, 2013, **42**, 845–856.
- 85 D. C. Teles-Ferreira, R. Borrego-Varillas, L. Ganzer, B. E. Nogueira Faria, C. Manzoni, S. De Silvestri, A. Nenov, I. Conti, M. Garavelli, G. Cerullo and A. M. de Paula, *EPJ Web Conf.*, 2019, **205**, 10005.
- 86 A. Weigel, A. L. Dobryakov, M. Veiga and J. L. Perez Lustres, *J. Phys. Chem. A*, 2008, **112**, 12054–12065.
- 87 V. I. Prokhorenko, A. Picchiotti, M. Pola, A. G. Dijkstra and R. J. D. Miller, *J. Phys. Chem. Lett.*, 2016, **7**, 4445–4450.